remote sensing

MDPI

Article

Understanding How Low-Level Clouds and Fog Modify the Diurnal Cycle of Orographic Precipitation Using In Situ and Satellite Observations

Yajuan Duan and Ana P. Barros *

Department of Civil and Environmental Engineering, Duke University, Durham, NC 27708, USA; yajuan.duan@duke.edu

* Correspondence: barros@duke.edu; Tel.: +1-919-660-5539

Received: 26 July 2017; Accepted: 30 August 2017; Published: 2 September 2017

Abstract: Satellite orographic precipitation estimates exhibit large errors with space-time structure tied to landform. Observations in the Southern Appalachian Mountains (SAM) suggest that low-level clouds and fog (LLCF) amplify mid-day rainfall via seeder-feeder interactions (SFI) at both high and low elevations. Here, a rainfall microphysics model constrained by fog observations was used first to reveal that fast SFI (2–5 min time-scales) modify the rain drop size distributions by increasing coalescence efficiency among small drops (<0.7 mm diameter), whereas competition between coalescence and filament-only breakup dominates for larger drops (3–5 mm diameter). The net result is a large increase in the number concentrations of intermediate size raindrops in the 0.7–3 mm range and up to a ten-fold increase in rainfall intensity. Next, a 10-year climatology of satellite observations was developed to map LLCF. Combined estimates from CALIPSO (Cloud-Aerosol Lidar and Infrared Pathfinder Satellite Observations) and CloudSat products reveal persistent shallower cloud base heights at high elevations enveloping the terrain. The regional cloud top height climatology derived from the MODIS (Moderate Resolution Imaging Spectroradiometer) shows high-frequency daytime LLCF over mountain ridges in the warm season shifting to river valleys at nighttime. In fall and winter, LLCF patterns define a cloud-shadow region east of the continental divide, consistent with downwind rain-shadow effects. Optical and microphysical properties from collocated MODIS and ground ceilometers indicate small values of vertically integrated cloud water path (CWP < 100 g/m^2), optical thickness (COT < 15), and particle effective radius (CER) < 15 μm near cloud top whereas surface observed CER ~25 μm changes to ~150 μm and higher prior to the mid-day rainfall. The vertical stratification of LLCF microphysics and SFI at low levels pose a significant challenge to satellite-based remote sensing in complex topography.

Keywords: mountains; clouds; orographic precipitation

1. Introduction

In mountainous areas, low-level clouds and fog (LLCF) have significant implications on the regional hydrological cycle by affecting the diurnal cycle and spatial organization of precipitation and surface fluxes [1,2]. In cloud- or fog-dominated montane regions, cloud immersion and fog water are closely linked to ecosystem hydrology, nutrient budgets, and pollutant dynamics, as well as species distribution and abundance [3–7]. Based on National Climatic Data Center (NCDC) records between 1961 and 1990 [8], the Southern Appalachian Mountains (SAM) stands out in the continental US with dense fog frequently reported (>40 days/year at regional scale). The cloud forests of the SAM at relatively high altitude (above ~1500 m elevation) experience cloud immersion about 60–75% of the summer days, mostly occurring during morning hours [9]. In the SAM, and generally in tropical and mid-latitude montane cloud forests, frequent cloud immersion creates favorable conditions for direct

foliar water uptake (the direct absorption of water through leaves), enhances root uptake by improving top soil moisture, and reduces incoming shortwave radiation and the amplitude of the diurnal cycle of canopy temperature. Water from cloud immersion and fog has been found to contribute significantly to the overall plant water budget in the SAM, up to 31% throughout the entire summer growing period, especially for high-elevation plants [10]. Moreover, LLCF also modulates available photosynthetically active radiation, enhancing photosynthesis and leaf conductance, thereby leading to improved carbon uptake and water conservation of plants [11,12]. Mapping LLCF and understanding their role in the water cycle of mountain regions is therefore a critical research need.

Observations from raingauge and disdrometer networks in the SAM (Figure 1) show a complex relationship with elevation and landform that does not fit the classical orographic enhancement conceptual model with terrain elevation [13,14]. Instead, in situ data show strong west-east variability with small differences between rainfall accumulations at low and high elevations at annual time-scales, but large differences under strong synoptic forcing from event to event depending on whether LLCF are present either at high or low elevations, that is the reverse orographic enhancement effect [15]. One distinctive feature of the SAM rainfall is the existence of a mid-day rainfall peak in all seasons, which is similar to that observed at mid-elevations in the forested slopes of the central Andes and in tropical cloud forests [1,14,16]. Prat and Barros [16,17] reported number concentrations of small drops in the inner SAM up to two orders of magnitude higher than the values used in common parameterizations of rain drop size distributions (R-DSDs, e.g., Marshall-Palmer distribution among others). They also documented robust ridge-valley differences in the seasonal climatology of R-DSDs with larger drop sizes at lower elevations. Wilson and Barros [18] found that the microphysics of the mid-day rainfall peak at paired ridge-valley sites in the inner mountain region are characterized by very large number concentrations of small drops and light rainfall intensity in the presence of thick fog at both locations (concurrently or not) with large increases in the number of large drops under moderate and heavy rainfall conditions. Concurrent bottom-heavy radar reflectivity profiles further indicated that these microphysical changes took place within the lower 500 m suggesting seeder-feeder interactions (SFI) between rainfall aloft and low-level fog. This hypothesis was tested by Wilson and Barros [18] using a raindrop dynamics column model [19–21] modified to include fog. Due to the lack of in situ observations, they synthesized fog spectra from the literature for their model experiments and showed that increased coalescence efficiency between precipitating clouds aloft and thick fog in the inner SAM could explain the observed increase in rainfall rate and DSD modification.

The present study aims to generalize the quantitative understanding of how LLCF modify the diurnal cycle of orographic precipitation from local scales to regional-scale in the SAM using in situ and satellite observations. This encompasses characterizing SFI processes on the upwind slopes of the SAM with distinct hydrometeorology from the inner region, and the process chain by which the observed regional-scale organization of the diurnal-cycle emerges. The specific research objectives are two-fold: (1) to elucidate the physical mechanisms of rainfall amplification by LLCF at local scales, and (2) to elucidate the role of LLCF at regional-scale by demonstrating the spatial co-organization of the diurnal cycle of LLCF and orographic precipitation. First, microphysical observations of LLCF immersion are used to constrain a spectral model of rain dynamical microphysics to investigate how fast SFI can modify the R-DSDs on upwind slopes. Second, systematic analysis of satellite observations that enable mapping LLCF features during the observed all-season mid-day rainfall peak is conducted. Specifically, satellite observations from CALIOP (Cloud-Aerosol Lidar with Orthogonal Polarization) on the CALIPSO (Cloud-Aerosol Lidar and Infrared Pathfinder Satellite Observations) satellite (www.nasa.gov/mission_pages/calipso), from CPR (Cloud Profiling Radar) on the CloudSat satellite (www.nasa.gov/mission_pages/cloudsat), and from MODIS (Moderate Resolution Imaging Spectroradiometer) on the Aqua satellite (https://modis.gsfc.nasa.gov/) are used toward developing a satellite-based climatology and physical characterization of orographic LLCF regimes focusing on the Southern Appalachians (SA) using a general methodology that can be applied to mountainous regions elsewhere. A simple method to merge CALIPSO and CloudSat products was developed to improve

cloud base height (CBH) estimates and evaluated against ground ceilometer observations in the SAM. MODIS cloud top, optical, and microphysical properties are explored to map the spatial distribution of LLCF and further describe various aspects of LLCF characteristics over this region. The paper is organized as follows. Details of satellite products and surface observations (fog measurements and 10-year ceilometer observations), an introduction of the merging method using the CALIOP and CPR CBH, and a brief description of the rain microphysics column model are provided in Section 2. Section 3 presents the modeling study to address Objective 1, an evaluation of merged CBH estimates from CALIOP and CPR against in situ ceilometer observations, and the MODIS climatology of cloud top, optical, and microphysical properties of LLCF in the SAM. In Section 4, we discuss limitations of the current study and provide an overall assessment on the application of multi-satellite observations and model simulations to map LLCF distribution and SFI modulation of orographic precipitation. Finally, the main findings are summarized in Section 5.

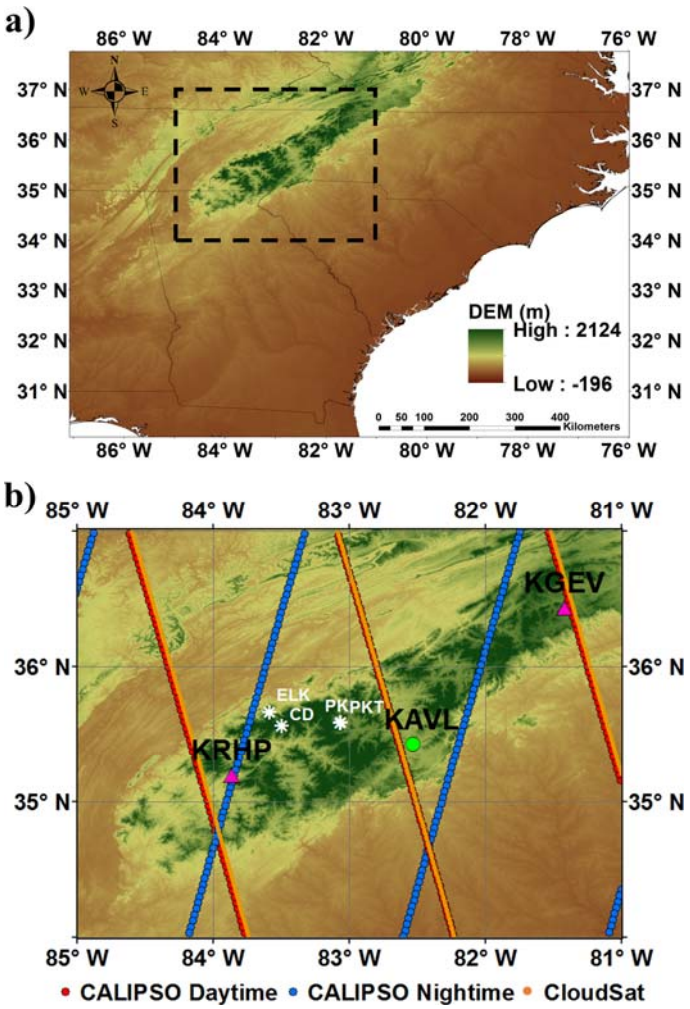

Figure 1. (**a**) Region of study (in the black box) in context of southeastern United States map; (**b**) Overview of Cloud-Aerosol Lidar and Infrared Pathfinder Satellite Observations (CALIPSO) and CloudSat overpasses over the study region. Note the CALIPSO daytime tracks are represented by red dotted lines and the nighttime ones by the blue dotted lines. The CloudSat daytime tracks are indicated by orange lines. From left to right, the three ground ceilometer stations are located at Andrews Murphey Airport (KRHP, marked by the pink triangle), Asheville Airport (KAVL, marked by the green circle), and Jefferson Ashe County Airport (KGEV, marked by the pink triangle). White asterisks denote the locations of four ground fog collectors at Elkmont (ELK), Clingmans Dome (CD), Purchase Knob (PK), and Purchase Knob Tower (PKT).

2. Materials and Methods

2.1. Satellite Products

Due to the sparse distribution of in situ measurement networks in remote mountainous areas, satellite-based observations provide an opportunity for long-term monitoring of regional cloud systems with wide spatial coverage. NASA's EOS (Earth Observing System) passive satellites have enabled global coverage of cloud observations, but their retrieval algorithms are unable to resolve cloud vertical structure, especially under multilayer scenarios [22,23]. The availability of satellite-based active sensors allows to investigate cloud structure directly including detailed vertical profiles, as well as their optical and microphysical properties at unprecedented resolutions [24,25]. Launched in 2006, CloudSat and CALIPSO aim to monitor the vertical distribution of clouds at high spatial resolution and to bring new insights on their evolution throughout the atmosphere [24,26]. CPR and CALIOP, the active sensors on CloudSat and CALIPSO, respectively provide a nadir view of vertical cloud profiles, complemented by the wide-view images from the MODIS instrument on the Aqua satellite. As part of the A-Train constellation, these three satellites maintain a close formation with each other, and are in nearly the same orbit with approximately fixed distance from each other. This flying array enables similar sampling volume of the atmosphere and facilitates the integration of their respective data sets. In April 2011, CloudSat experienced a severe battery anomaly and only daytime data are available after October 2011. Prior to the anomaly, CloudSat and CALIPSO maintained a spatial separation of the ground tracks within 1 km and a temporal difference of 15 s on average, trailing the Aqua satellite by approximately 60 and 75 s, respectively. The data analysis presented in this study was performed from June 2006 to October 2016, using 10 years of spaceborne measurements from CALIPSO, CloudSat, and MODIS.

CALIOP—The CALIOP is a two-wavelength (532 and 1064 nm) polarization-sensitive Lidar, that provides high-resolution vertical profiles of aerosols and clouds [25]. CALIOP profiles have a circular footprint of ~70 m in diameter with vertical resolution of 30 m, and are collected every ~333 m along the track. This highest resolution is only available for those portions of the profiles lower than 8.2 km, and the data are recorded at 1 km horizontal and 60 m vertical resolution above 8.2 km. The CALIPSO Level 2 (version 3) cloud layer products are also derived on horizontal grids of 1 km and 5 km. The layer products include number of vertical cloud layers, cloud top height (CTH) and CBH for each of these layers (up to five layers per profile). Information on Level 2 processing can be found in the CALIPSO algorithm theoretical basis documents (ATBDs), Young et al. [27], and Winker et al. [28]. All data products and ATBDs are available from the Atmospheric Science Data Center at NASA Langley Research Center (https://eosweb.larc.nasa.gov/). The main documented limitations of CALIOP are: (1) the laser pulse suffers complete attenuation beyond optical depth of ~5 from the top layer, thus likely leading to overestimated cloud base retrievals [29]; and (2) the solar background signal dominates the total background signal in daylight profiles, decreasing CALIOP sensitivity to optically thin clouds [30].

CloudSat—The CPR is a nadir-looking 94 GHz millimeter-wavelength radar and enables matching of CALIOP observations to collect similar sampling volumes with slight time and space offsets between CloudSat and CALIPSO as part of the A-Train constellation [24]. CPR backscattered pulses are resampled to generate range bins of 240 m vertical resolution and the profiles are produced every 1.1 km along the orbit track with a horizontal footprint of 1.8 km along track and 1.4 km across track [31]. Herein we use the CloudSat 2B-GEOPROF (geometrical profile product), including information on the cloud mask and radar reflectivity [32]. To differentiate clouds and other hydrometeors from instrument noises, a cloud mask is created to identify the presence of hydrometeors and to estimate the confidence levels of hydrometeor detection. Its value ranges from 0 to 40, with higher values indicating lower probability of false detections. In this study, CPR bins with the cloud mask level exceeding 20 are considered as cloudy, corresponding to a false-positive probability of less than 5% [26]. Details about the hydrometeor mask algorithm are described in Marchand et al. [32]. The 2B-GEOPROF data set

can be acquired from the CloudSat data processing center (http://www.cloudsat.cira.colostate.edu/). The main documented limitations of CPR are (1) low sensitivity of the radar pulse in the lowest 1 km above the surface, likely producing spurious echoes due to the ground clutter effects; (2) the detection threshold of CPR is −30 dBZ, thus making it unable to capture some fraction of high thin cirrus and non-precipitating shallow boundary layer clouds; and (3) the relatively coarse horizontal and vertical resolution likely result in missing small-scale clouds [33]. Thus, bins in the bottom 1 km (lowest four bins) above the surface were excluded from the analysis to avoid ambiguity from reduced CPR sensitivity.

MODIS—Maintaining a close formation with CALIPSO and CloudSat, the Aqua satellite carries a passive sensor MODIS, which operates in the visible and infrared regions of the spectrum with measurements at 36 wavelengths from 0.4 to 14.5 μm [34]. Since February 2000, MODIS has provided global distributions of clouds (aerosols) and their physical and optical properties with a wide-swath scanner (2330-km cross-track and 10-km along-track at nadir) and a scan angle of ±55°. In this study, daytime MODIS cloud optical and microphysical properties in Collection 6 (C6), including cloud water path (CWP), cloud optical thickness (COT), and cloud particle effective radius (CER), are obtained from the Level 2 MYD06 product at 1 km horizontal resolution [35]. MODIS cloud mask product (MYD35) is also used in this study and it reports four confidence levels of cloudiness conditions (confident cloudy, probably cloudy, probably clear, and confident clear) [36]. The MODIS C6 data can be retrieved from the NASA Level 1 and Atmosphere Archive and Distribution System (https://ladsweb.nascom.nasa.gov/). Leveraging collocated CALIOP observations, significant refinements and extensive testing have been put into the C6 algorithm development. In C6, a modified CO_2-slicing method is applied to retrieve the cloud top pressure (CTP) for mid- and high-level clouds based on cloud emissivity ratios from multiple bands (bands: 29–32). Compared to collocated CALIOP CTH of single-layer clouds, substantial improvements have been shown in the overall global detection skill in semi-transparent cirrus and low-level liquid phase clouds in C6 versus C5 [37]. Earlier studies indicate that the minimum optical depth for cloud detection in MODIS is 0.4 [38], whereas the sensitivity of CALIOP signals is sufficient to detect thin cirrus with optical depths of 0.01 or less [39].

Both CALIOP and CPR measurements can be used to infer cloud phases and other microphysical properties from the information on the polarization of the backscattered signals at different frequencies [40]. Because of different wavelengths, CALIOP (visible and near-infrared) and CPR (microwave) have distinct sensitivities to cloud particle sizes, thus resulting in different characteristics of bias and estimation errors. The CPR is capable of penetrating optically thick hydrometeor layers, and has higher sensitivity to large particles existing in cloud top regions [41], but suffers significant attenuation of radar signals in moderate to heavy rainfall [42]. The Lidar is superior in detecting tenuous and optically thin clouds, which are below radar reflectivity thresholds due to its limited sensitivity to small cloud droplets and ice particles. However, Lidar observations suffer strong signal attenuation beyond an optical depth of about 3, especially at lower levels due to opaque thick tropospheric clouds and multilayer clouds above [43]. Integration of CPR and CALIOP observations should help minimize the respective cloud detection deficiencies of each sensor by leveraging their strengths. Nevertheless, difficulties still remain in detecting shallow liquid clouds (weakly reflective to the radar and/or below 1 km) beneath higher-level opaque clouds that completely extinguish Lidar signals [26].

2.2. Merging Methodology Using CALIOP and CPR

Given the complementary nature of CALIOP and CPR, the synergistic use of these two sensors can potentially provide a complete vertical profile of cloud layering and work to minimize the deficiencies in detecting LLCF. A strategy to merge CALIOP and CPR measurements designed to extract maximum information regarding the occurrence of hydrometeor layers is outlined next. Because tenuous and broken clouds at low-levels are likely to be missed by the CALIOP due to its small sampling area and strong attenuation of Lidar signals, thereby decreasing the chance of LLCF detection, horizontal

averaging of the CALIOP Level 2 CBH at 333-m resolution is necessary before merging the products of the two active sensors. Instead of simple averaging, the algorithm developed by Zhang et al. [44] was adopted to account for clouds from different layers or different parts of the same layer. The schematic diagram in Figure 2 illustrates the algorithm workflow that starts with preprocessing the CALIOP data. The CALIOP CBH (CBH-L) is chosen as the smaller value of non-null CBHs determined using the following two approaches: (1) spatial and temporal geolocation match to the center of the sampling area within the CALIOP footprint (333-m); and (2) horizontal averaging was conducted over the sampling box following the procedure as described in Zhang et al. [44]. The CPR CBH (CBH-R) is determined as the lowest bin height with cloud mask level greater than 20 and matched to the center of the sampling area within the CPR footprint (1.4 km). Finally, the merged CBH for the sampling area is chosen as the smaller value of CBH-L and CBH-R. Overall, this framework not only maintains the superior detection skill of each sensor when both measurements are available, but also enables detection when either signal is unavailable.

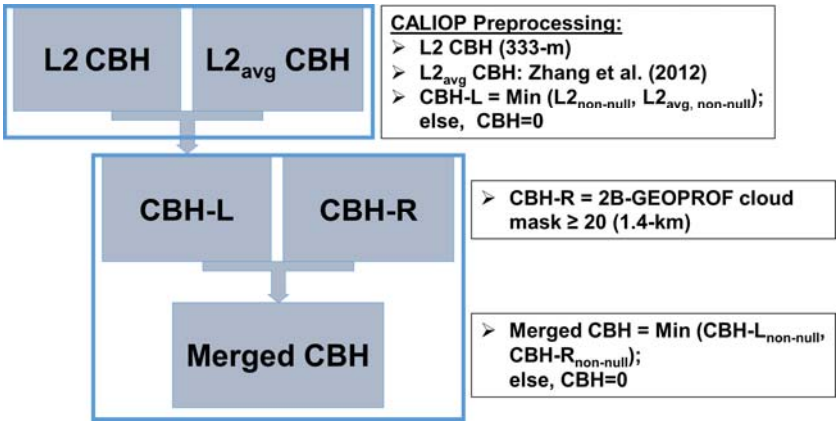

Figure 2. Schematic of merging the CALIOP cloud base height (CBH) using the L2 333-m cloud layer product and the Cloud Profiling Radar (CPR) CBH from the geometrical profile product (2B-GEOPROF).

2.3. Surface Observations

2.3.1. Fog Observations

Over the western ridge of the SAM and the inner mountain region, fog collectors were deployed at four ground stations (marked by white asterisks in Figure 1b) for different sampling periods during June 2013–December 2015. Descriptions about these sites and the corresponding observation periods are summarized in Table 1. The fog collectors used in this study are designed and manufactured by Professor James Juvik at University of Hawaii. Details about the fog collectors are described in Juvik and Nullet [45] and Wilson and Barros [15]. Figure 3 shows the diurnal and seasonal cycles of fog occurrences sampled by the fog collectors at Purchase Knob (PK), Purchase Knob Tower (PKT), and Clingmans Dome (CD). The observations at Elkmont (ELK) are not shown here due to its shorter sampling period. Over the inner mountain region, longer records (~two years) were reported at PK and PKT, which are approximately 0.7 km apart. As noted in Figure 3a,b, distinct diurnal features are manifest at these two nearby sites. PK, which is at one ridge location with widely open area, reveals a mid-day peak of fog occurrences in winter associated with advection fog whereas weak diurnal variations are indicated for other seasons. PKT, an open area location surrounded by dense forests, shows less frequent fog occurrences around the mid-day maximum in the winter season while a pronounced morning peak of radiation fog is apparent in the warm season (spring and summer). On the western ridges, fog observations at CD in late spring and summer of 2014 indicate a strong diurnal variability with peaks at early morning and late night as a result of nocturnal cooling near

the ground surface (radiation fog). The remarkably high frequency of fog occurrences at CD supports previous reports that this site CD is constantly immersed in the cloud deck [15].

To characterize fog microphysical properties in the SAM, a meteorological particle spectrometer (MPS, manufactured by Droplet Measurement Technologies, Inc., Boulder, CO, USA) was deployed along the fog collector at ELK site during September–December 2015. The MPS measures droplet concentrations, sizes, shapes, and fall velocities over the diameter size range from 12.5 μm to 1.56 mm in 62 evenly spacing bins (25 μm resolution) [46]. The MPS uses a collimated laser beam of light (a linear array of 64 photodiodes) between two vertical arms to measure the shadow images of falling particles that form on the array [47]. Significant improvements have been made in the MPS to mitigate measuring issues under windy conditions and to provide high resolution of fall velocities better than 0.01 mm s^{-1} [46]. Other collocated instruments at Elkmont include a METEK Micro Rain Radar (MRR), operating at 24 GHz (K band) with the range-gate resolution of 100 m up to 30 vertical levels in the atmosphere and sensitivity to rain rates of 0.01 mm h^{-1}; a tipping bucket rain gauge (RG) with measurement resolution of 0.1 mm tip^{-1}; a Vaisala weather station (WXT520) recording local meteorological conditions (e.g., wind speed, wind direction, relative humidity, and temperature) every 1-s.

Table 1. Descriptions of the fog collectors and their deployment periods in the Southern Appalachian Mountains (SAM).

Site Name	Latitude	Longitude	Elevation (m)	Fog Observation Period
Purchase Knob (PK)	35.586	−83.073	1495	1 June 2013–19 May 2015
Purchase Knob Tower (PKT)	35.588	−83.065	1485	4 July 2013–5 October 2015
Clingmans Dome (CD)	35.562	−83.497	1956	1 June–10 September 2014
Elkmont (ELK)	35.665	−83.590	634	25 September–10 December 2015

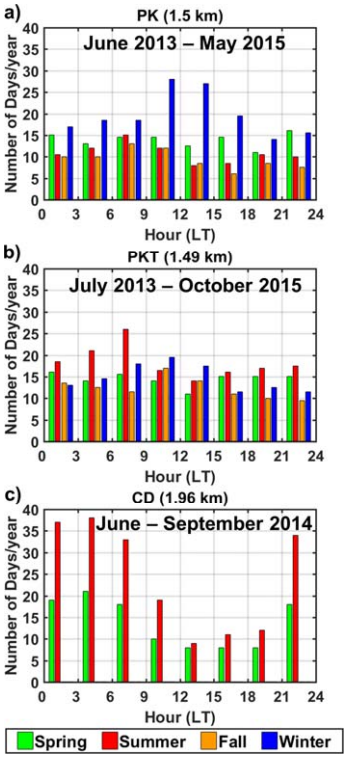

Figure 3. Diurnal cycles of fog occurrences in each season (spring: April-May-June, summer: July-August-September, fall: October–November–December, and winter: January–February–March) sampled by fog collectors at PK (**a**), PKT (**b**), and CD (**c**). Note the elevation of each site is denoted in parentheses after its name and the corresponding observation period is indicated at the top of each plot.

2.3.2. Ceilometer Observations

The Automated Surface Observing System (ASOS) equipped with automated laser ceilometers is a valuable source of long-term cloud observations in the United States since 1992 [48]. Routine observations generally report cloud cover, sky condition, cloud type, CBH, and visibility. There are currently more than 900 ASOS sites in the United States [49]. The Automated Weather Observing System (AWOS) is operated and controlled by the Federal Aviation Administration (FAA), recording similar surface observations at a 20-min interval. The 5-min ASOS and 20-min AWOS data are archived by the National Oceanic and Atmospheric Administration (NOAA) NCDC (http://www.ncdc.noaa.gov/).

At the ASOS/AWOS unit, the CBH is estimated from vertical profiles up to 3.6 km (~15 m vertical resolution) above the surface and calculated from every 30-s sample during the most recent 30-min observational periods (with the last 10 min of data doubly weighted). Note three different layers can be detected at a time. The cloud height indicator sensor uses a vertical-pointing laser beam (0.9 μm) to track the time interval between pulse transmission and reception reflected from cloud base to determine the CBH. Moreover, local radiation fog is also reported by the co-located visibility instrument. Common issues with ceilometer CBH estimates are: (1) the algorithm cannot respond fast enough to detect rapidly changing sky conditions; (2) the laser is very sensitive and occasionally detects invisible moist layers before visible clouds form; and (3) sometimes sharp inversions in very cold winter weather, may cause false detection of clouds. Nevertheless, ceilometers provide well-qualified and consistent ground observations of cloud vertical structure at low altitude.

The region of study spans the SA (34° N–37° N, 85° W–81° W) as depicted in Figure 1. There are about 9 ASOS/AWOS stations available over the study region though only 3 stations (denoted by the green circle and pink triangles in Figure 1b) are located along or in the vicinity of the CALIPSO/CloudSat tracks (denoted by red/blue, and orange dots). For daytime overpasses, we employed the 5-min ASOS dataset from the Asheville Airport (KAVL) at an elevation of 654 m above mean sea level (MSL) and the 20-min AWOS dataset from the Jefferson Ashe County Airport (KGEV) at an elevation of 969 m MSL; for nighttime overpasses, the 20-min AWOS dataset from the Andrews Murphy Airport (KRHP) at an elevation of 520 m MSL was used. At these surface sites, CBH is the primary observation used in this study. First, we examined the seasonal distribution of the cloud cover using the ceilometer CBH at the first layer and the diurnal cycle of fog (in local time, LT) using visibility measurements during June 2006–October 2016. Figure 4 displays the frequency distribution of CBH (in the left panel) and the diurnal cycle of fog occurrences (in the right panel) at each site in each season. We can see that more frequent LLCF are observed at all three stations in the warm season (spring and summer) compared to the cold season (fall and winter). However, distinct features of cloud and fog regimes are also evident at the three ground observation stations. At the low-elevation sites (KAVL and KRHP), the CBH distribution peaks around 1–2 km above ground level (AGL). At the high-elevation site (KGEV), the frequency reaches the maximum around 0.5–1.5 km AGL. Thus, lower cloud bases tend to be formed over the ridge location compared to valley stations. In terms of fog occurrences, corresponding to a visibility range shorter than five eighth Statute Miles (SM), the two valley sites (KAVL and KRHP) experience persistent radiation fog in the early morning of all seasons, whereas the ridge station (KGEV) records more frequent morning fog in the warm season than the two valley sites and the diurnal cycle of fog in the cold season is uniformly distributed at KGEV. Despite a large spatial variability of LLCF over the SAM, these three stations serve as the ground truth for the multi-year climatology study using satellite measurements as described in Section 3.2.

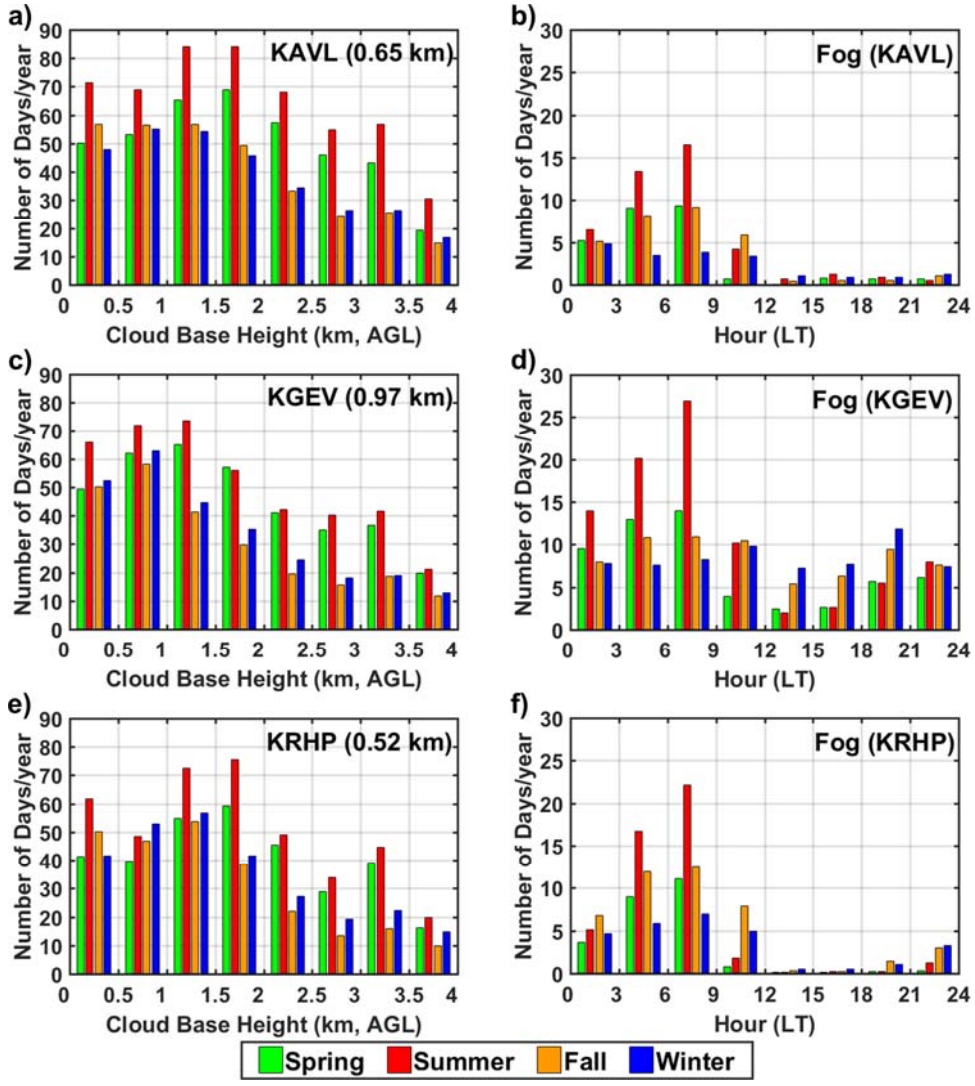

Figure 4. (**Left**) Seasonal histograms of ceilometer cloud base heights (CBHs) at KAVL (**a**), KGEV (**c**), and KRHP (**e**) during June 2006–October 2016. Note the elevation of each site is denoted in parentheses after its name; (**Right**) Seasonal and diurnal cycles of fog occurrences (visibility < 5/8 Statute Miles) at the corresponding ceilometer sites (KAVL: **b**; KGEV: **d**; KRHP: **f**) during the same period. Note the spring season represents April-May-June, the summer season represents July-August-September, the fall season represents October-November-December, and the winter represents January-February-March.

2.4. Column Model Description

A dynamical microphysics bin model that simulates the evolution of raindrop microphysics between cloud base and the ground surface (rain shaft) for warm rainfall events can be used to investigate the collisional drop-drop interactions between light seeder rainfall and local feeder fog [19,20]. This column model explicitly solves the stochastic collection equation-stochastic break equation (SCE-SBE) using a number and mass conservative scheme on a discretized bin grid. The discrete formulation of the SCE-SBE equation in the ith bin ($i = 1, 2, \ldots, nbin$) is written as

$$\begin{aligned}\frac{dN_i(z,t)}{dt} + V_i \frac{dN_i(z,t)}{dt} &= S_i(z,t) \\ &= \sum_{\substack{j,\ k \\ x_{i-1} \le (x_j + x_k) \le x_{i+1}}}^{j \ge k} \left(1 - \tfrac{1}{2}\delta_{j,k}\right) \eta C_{j,k} N_j(z,t) N_k(z,t) \\ &\quad - N_i(z,t) \sum_{k=1}^{nbin} C_{i,k} N_k(z,t) \\ &\quad + \tfrac{1}{2} \sum_{j=1}^{nbin} \sum_{k=1}^{nbin} N_j(z,t) N_k(z,t) B_{i,k} \kappa_{i,j,k} - N_i(z,t) \sum_{k=1}^{nbin} B_{i,k} N_k(z,t)\end{aligned} \quad (1)$$

where the first term on the left-hand side of the equation describes time rate of change in the droplet number concentration N_i (z, t) at height z and time t, the second term accounts for the falling of drops at a velocity V_i. The source term S_i (z, t) represents the net gain from coalescence-breakup dynamics, which is expressed by the four terms at the right-hand side of the equation. From left to right, they are the production of droplets resulting from coalescence of smaller drops, the removal of droplets resulting from coalescence with other droplets, the gain of droplets due to breakup of larger drops, and the loss of droplets due to their breakup. One distinct aspect of the model is the explicit incorporation of bounce and distinct modes of breakup (neck/filament, sheet, crown and disk) [15,18,50,51] using a *We-p* parameterization of regimes of collision outcomes after Testik et al. [52] and Prat et al. [21], where *We* is the Weber number and p is the ratio of the small to the large diameter of two colliding raindrops (see Figure S1 in the supplementary material).

Finally, the rain rate at height z and time t is expressed as

$$RR(z,t) = \frac{3600}{\rho_w} \sum_{i=1}^{nbin} N_i(z,t) m_i V_{rel}(z) \quad (2)$$

$$V_{rel}(z) = V_i - V_{air}(z) \quad (3)$$

where m_i is the characteristic mass (g) of drops in the ith bin, the relative velocity V_{rel} (z) is calculated as the difference of the fall velocity of drops in the ith bin V_i and the mean air velocity V_{air} (z) at height z (downdrafts are denoted by positive signs and updrafts in negative signs), and ρ_w is the density of water (=1 g cm^{-3}).

The radar reflectivity (*ZDBZ*) is computed as

$$ZDBZ(z,t) = 10log_{10}\left(\sum_{i=1}^{nbin} N_i(z,t) D_i^6\right) \quad (4)$$

where *Di* is the characteristic diameter of drops in the ith bin. Note the dependence of reflectivity on D^6 corresponding to a factor of ~0.001 between 1 and 3 mm drop diameters everything else being equal, which is illustrative of the strong nonlinear decrease in the sensitivity of radar measurements for small drop sizes.

3. Results

3.1. Seeder-Feeder Interactions

As discussed in Section 1, the SAM experience mid-day light rainfall throughout the year that peaks before convective activity develops in the mid and late-afternoon [14,18]. Elsewhere, mid-day light rainfall does not reach the ground due to evaporation in the warm season (e.g., Himalayas) [53]. By contrast, mid-day rainfall in the SAM can reach hourly rates similar to convective precipitation (i.e., >10 mm/h). Microphysical and radar observations indicate significant enhancement of number concentrations across the R-DSD spectrum, and in particular in the number of large drop sizes that reach the surface [15,18]. Light rainfall can potentially interact with LLCF (i.e., SFI)

consequently leading to significantly enhanced surface rainfall as documented by Prat and Barros [16] and Wilson and Barros [15,18]. Wilson and Barros [18] resorted to ground observations and modeling to demonstrate the importance of LLCF in amplifying precipitation in the inner SAM via SFI, including the mid-day peak and the evening ridge-valley gradients. They relied on typical values of fog distributions (droplet number concentrations, liquid water content) from the literature to define fog microphysics, as observations were not available at that time. In this study, the local fog DSDs (F-DSDs) observed by the MPS at ELK was used to investigate the physical mechanisms of low-level precipitation enhancement induced by the SFI on the western (upwind) slopes of the SAM under strong mountain-valley wind conditions.

In the early morning of 1 October 2015, large number concentrations of small drops (12.5–37.5 μm) were recorded by the MPS at ELK, indicating the presence of radiation fog (Figure 5a). The droplet effective radius (r_e, see Equation (A1) in Appendix A), derived from the MPS droplet size distributions remained relatively constant (~25 μm) in the morning and suddenly increased up to 375 μm around mid-day (shaded area in Figure 5b) enhanced by low level moisture convergence [54]. The mean liquid water content (LWC, see Equation (A2)) around the mid-day peak (11:00–14:00 LT) is 0.09 g/m^3 (not shown here). In the early afternoon, upper-level precipitation approached the site. Steeper reflectivity gradient toward the surface was observed by the MRR (Figure 5c), suggesting low-level amplification of the rainfall. This case is ideal to investigate SFI under light rainfall conditions representative of the persistent mid-day LLCF and rainfall on the western ridges of the SAM.

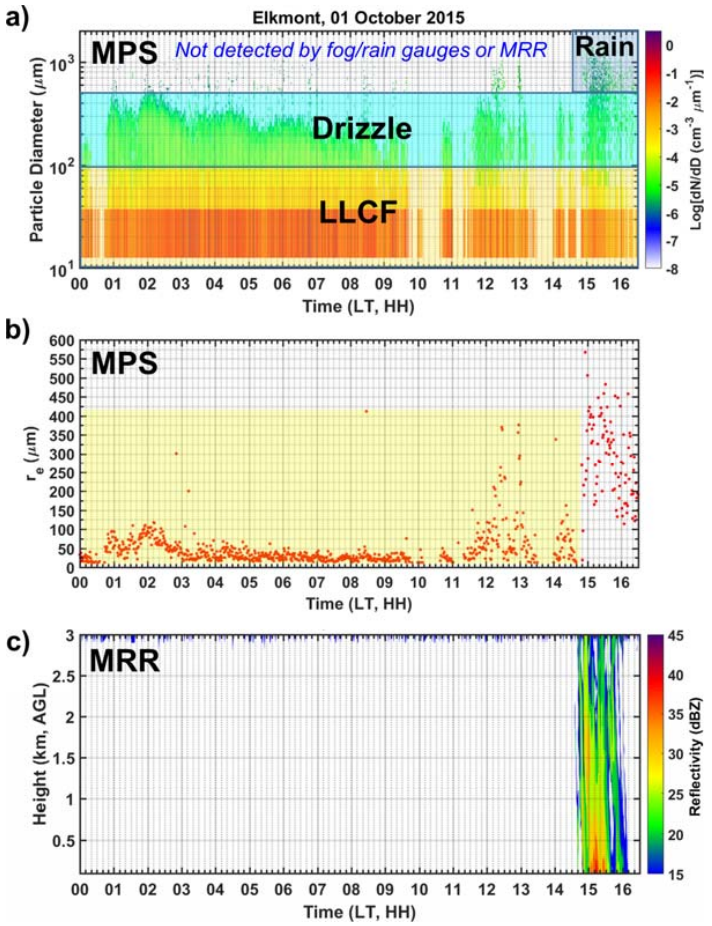

Figure 5. Time series of drop size distributions (**a**) from the meteorological particle spectrometer (MPS), droplet effective radius (r_e; **b**) derived from the MPS spectra, and reflectivity profiles (**c**) from a collocated Micro Rain Radar (MRR) at Elkmont on 1 October 2015. Note the shaded area in (**b**) highlights the period of fog presence.

3.1.1. Model Evaluation

Using the column microphysics model as described in Section 2.4, simulations for this event were set up from 14:50–16:00 LT and the model was run on an optimized irregular grid of 60 bins with diameters ranging from 10 μm to 6.2 mm [18]. The initial and top boundary conditions can be retrieved from the MRR observations. At the initial time, R-DSDs were derived from 30 levels of MRR reflectivity (100-m resolution) and imposed at the corresponding positions in the simulated vertical column. The dynamic top boundary condition (TBC) was updated every 60 s introducing a new R-DSD based on the MRR reflectivity measurements at the column top. The time step (1 s) and vertical resolution (10 m) are maintained constant during the simulation period. The TBC height was prescribed at 1300 m AGL based on the MRR profiles and to minimize lateral advection effects that are not represented in the model as well as ice microphysics that have a negligible influence on the rainfall evolution in the column. The selection of TBC height and the retrieval of R-DSDs from MRR reflectivity observations are detailed by Prat et al. [55] and Wilson and Barros [18]. In Wilson and Barros [18], a comprehensive review of the literature was conducted toward selecting appropriate F-DSDs, which were transferred and scaled to meet water budget requirements locally. Herein, we rely for the first time MPS observations to derive local F-DSDs just before the onset of a rainfall event. For six different periods (1, 10, 13, 15, 17, 20 min) before 14:50 LT, the F-DSD was obtained by averaging the MPS droplet spectra below 50 μm (maximum diameter for a fog droplets) and fitted by a negative exponential distribution (see Equation (5)) using least-squares minimization.

$$\frac{dN}{dD} = N_0 e^{-\Lambda D} \tag{5}$$

wherein N_0 (cm^{-3} μm^{-1}) represents the intercept and Λ (μm^{-1}) represents the slope. The fitting parameters for six averaging periods and the corresponding LWC (see Equation (A2)) are summarized in Table 2 and the resulting F-DSD spectra are shown in Figure 6a. Note an additional run was conducted by including droplet sizes up to 100 μm in fog spectra #2a. Next, several simulations were conducted assuming a uniform fog distribution of 400-m depth in the atmospheric column from 15:00–15:30 LT. Note that the timing and depth of fog were determined based on the observed reflectivity profiles that indicate stronger reflectivity gradients toward the surface (bottom heavy reflectivity profiles) during 15:00–15:30 LT within 400 m above the ground (see Figure 5c). With each F-DSD (Figure 6a) as model input, the cumulative rainfall is evaluated against the precipitation observations from the surface instruments (RG and MRR) at ELK, as shown in Figure 6b. Herein "MOD-SFI" refers to model output with the presence of fog, thus activating SFI between the falling raindrops from an upper-level seeder source and small droplets in the feeder fog; "MOD-NO FOG" refers to the simulation without fog.

Table 2. Fitting parameters of the negative exponential distribution characterizing the fog droplet spectra and their liquid water content (LWC) for different averaging periods before the onset of the rainfall event on 1 October 2015. Note N_0 represents the intercept and Λ represents the slope.

	Avg. Period	D_{max} (μm)	N_0 (cm^{-3} μm^{-1})	Λ (μm^{-1})	LWC (g/m^3)
FOG #1	1 min	50	0.59	0.11	0.0104
FOG #2a	10 min	50	0.37	0.11	0.006
FOG #2b	10 min	100	0.37	0.11	0.0074
FOG #3	13 min	50	2.15	0.17	0.0064
FOG #4	15 min	50	4.37	0.18	0.0101
FOG #5	17 min	50	3.75	0.19	0.0085
FOG #6	20 min	50	2.95	0.18	0.0078

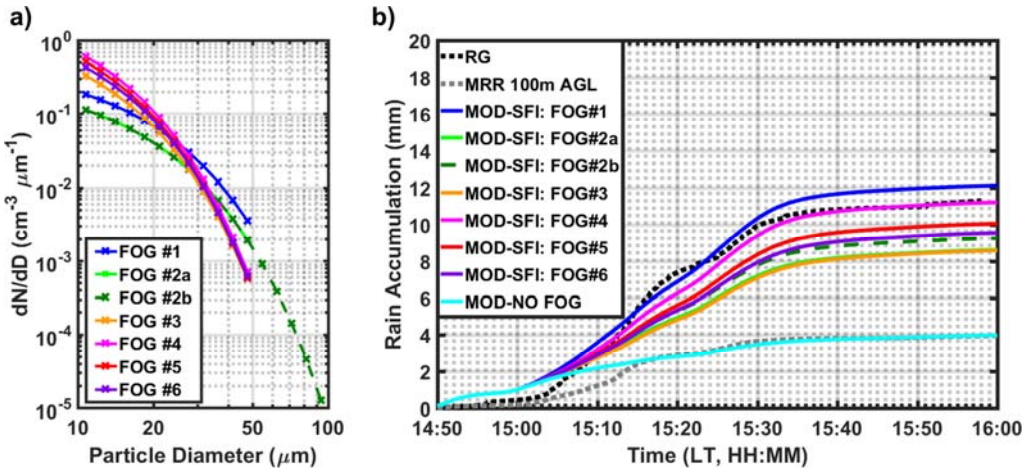

Figure 6. (**a**) Fog droplet spectra using six averaging periods of the MPS data before 14:50 LT (details about the spectra can be referred to Table 2); (**b**) Simulated cumulative rainfall with each spectrum used as the fog input in the model, compared to observations from the raingauge (RG, black dotted line) and MRR (grey dotted line). "MOD-SFI" indicates model simulations with the presence of fog, thus activating seeder-feeder interactions (SFI). "MOD-NO FOG" indicates the model simulation without fog.

When fog is taken into account, the simulated rain accumulation near the surface (10 m AGL) is comparable to the RG measurement (black dotted line in Figure 6b), which is considered as the ground truth. In particular, the simulation results with fog spectra #4 (15 min averaging period and LWC = 0.01 g/m^3 in Table 2, pink lines in Figure 6) achieve the best agreement with the overall rainfall accumulation reported by the RG at the end of the simulation period (70 min). As expected, the simulated rainfall using FOG #2b (with larger drops included in the fog spectra, indicated by the darker green dashed line) is slightly increased compared to the results from FOG #2a (indicated by the light green line). Note that the simulated rainfall accumulation without fog are consistent with the corresponding MRR rainfall observations at the first gate (100 m AGL, grey dotted line in Figure 6b), and both of them fail to capture the enhanced rainfall measured at the surface induced by the SFI. This is because the MRR reflectivity-rainfall estimation software provided by the manufacturer relies on incorrect assumptions, and therefore we use reflectivity alone for subsequent analysis. The rain accumulation at the beginning of the event (14:50–15:06 LT) is slightly overestimated by all the model simulations as compared to the surface observations from the RG and MRR. This overestimation error can be explained by comparing the reflectivity profiles from the MRR and the model results with the optimal fog input (MOD-SFI: FOG #4) in Figure 7. Within the height of TBC (1.3 km AGL, indicated by the thick black line in Figure 7a), a large amount of raindrops was falling through the simulation column around 14:52 LT, however, a discontinuity in the vertical structure of reflectivity profiles appeared around 15:00 LT below the TBC, which is likely caused by the advection of falling raindrops by the horizontal wind away from the MRR location (see surface wind speed in Figure 7c). By contrast, simulated reflectivity profiles (Figure 7b) show a continuous structure toward the surface around the same time, as horizontal wind is not taken into account in the column model. This results in stronger reflectivity in the simulation column during 15:00–15:06 LT as compared to the MRR observation. In general, the model simulation with SFI active captures well the temporal variations in reflectivity intensity at low levels, especially below 400 m AGL. Another consideration is the time lag between MRR reflectivity profile (nearly instantaneous) and the travel time of the transient R-DSD from the TBC height to the surface is ~2–5 min due to the spread in the distribution of fall speeds (i.e., small drops travel much slower than larger drops). Nevertheless, the reflectivity peak near the surface around 15:12–15:15 LT is not reproduced by the column model. Because the wind is relatively calm at this time (Figure 7c), there is less variability in the column control volume over which the MRR is

profiling, and wind artifacts are smaller, and thus these measurements are expected to better capture the vertical structure of rainfall.

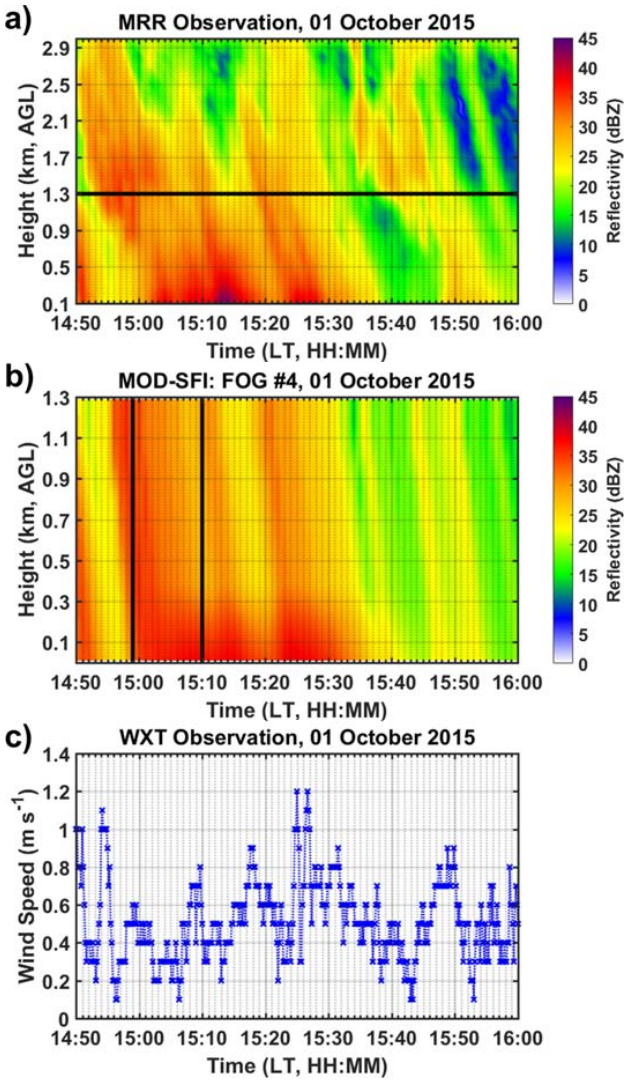

Figure 7. Time series of observed reflectivity (**a**) from the MRR, simulated reflectivity (**b**) with the presence of fog (FOG #4, see its spectrum in Figure 6a) during 15:00–15:30 LT, and surface wind speed (**c**) observed by the weather station (WXT). The black horizontal line in (**a**) marks the top boundary level at 1.3 km AGL. The black vertical lines in (**b**) mark 14:49 LT and 15:10 LT, which will be discussed in later figure.

The model simulates a column with winds at rest, and the temporal variability of fog microphysics proper is not represented in the model. For example, one important low-level process absent from the model representation is turbulence, which can play a significant role in fog dynamics by increasing the collision rate of droplets, thus significantly enhancing the efficiency of collision-coalescence process in fog microphysical processes [56,57]. Notwithstanding the approximations in the model and the limitations in the observations, the improved model prediction of rain accumulation (with fog spectra #4) against the simulation without fog is ~8 mm that is 65% of the total RG accumulation. Similar rainfall enhancement was captured in long-term paired fog and rainfall observations at all locations marked in Figure 1b as well as elsewhere across the SAM by contrasting paired high and low elevation observations [15,18,58]. These results highlight the remarkable contribution of LLCF to the enhanced rainfall intensity in agreement with the observations.

3.1.2. SFI Microphysics

To probe the impact of SFI on drop microphysics, the quantitative contribution of coalescence (first two terms on the right-hand side of Equation (1)) and breakup (last two terms on the right-hand side of Equation (1)) to changes in droplet number concentrations at three different heights (350-, 150-, 10-m AGL) are shown at 14:59 LT (before the activation of SFI) and at 15:10 LT (after the SFI have been going on for ten minutes) as illustrated in Figure 8. For light rainfall without "feeder" fog (14:59 LT, Figure 8a), coalescence dominates over breakup for drops smaller than 0.6 mm. At 15:10 LT (Figure 8b), the dominant role of coalescence over breakup shifts to small drop sizes ranging from 0.01 to 0.05 mm in diameter, indicating intensive interactions between feeder fog droplets (10–50 μm) and seeder rain drops (>100 μm) at low-levels. Further, coalescence effectively behaves as a collection mechanism with the much larger seeder drops sweeping the small fog droplets in their path [50] as expressed by net losses in number concentrations at 15:10 LT that are substantially larger than at 14:59 LT by approximately six orders of magnitude. As expected, persistent coalescence leads to an increased production of small raindrops (0.2–0.7 mm in diameter, Figure 8d) at 10 m AGL.

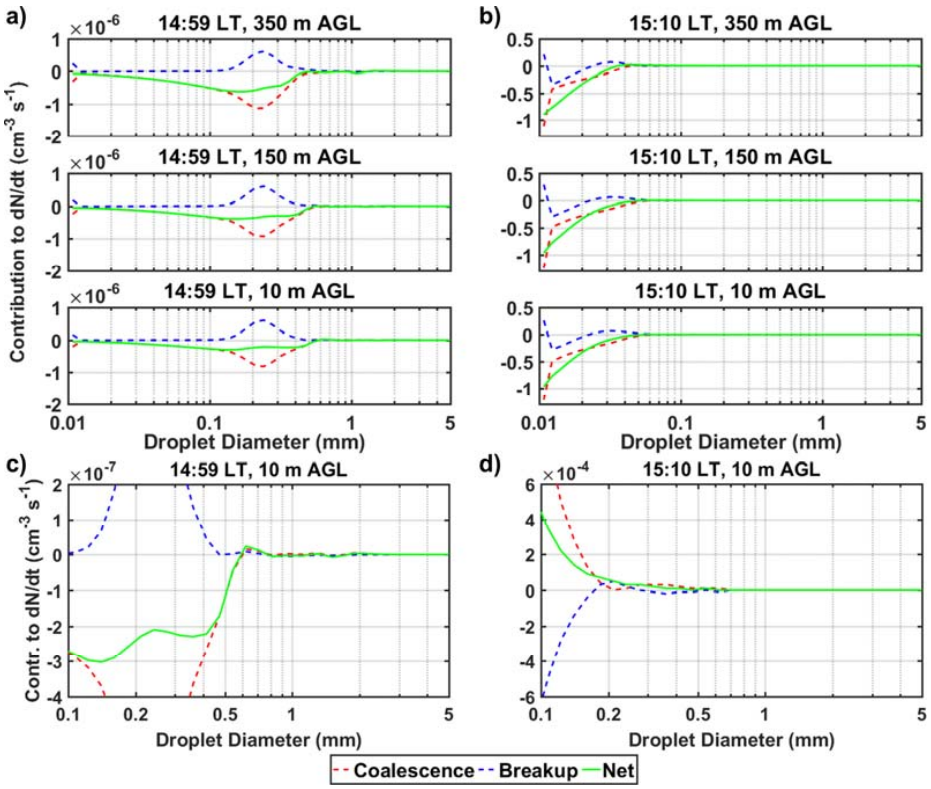

Figure 8. (**Top**) Contribution of coalescence and breakup processes to changes in simulated droplet number concentrations at three different heights (350-, 150-, 10-m above ground level (AGL)) in the simulation column before (14:59 LT; (**a**)) and after (15:10 LT; (**b**)) the activation of SFI in the model. (**Bottom**) Enlarged plots for 14:59 LT (**c**) and 15:10 LT (**d**) at 10 m AGL.

This effect is also manifest in the temporal evolution of the R-DSDs within the fog layer proper (400 m), as shown in Figure 9b–d. As a result of enhanced coalescence efficiency, the number concentrations of small raindrops (0.2–0.7 mm) at 15:10 LT (marked by the second vertical line in Figure 9a–d) are significantly higher than the ones at 14:59 LT (marked by the first vertical line in Figure 9a–d) by one to two orders of magnitude. This effect propagates across the spectrum, as the increase in the number of small raindrops later contributes to the increase in the number and efficiency of collisions between small diameter ($d2 < 0.6$ mm) and larger diameter drops ($d1$). As illustrated in

Figure S1a, the large number of collisions for low $p = \frac{d2}{d1}$ moves the collision outcomes dynamics from Regime II that is dominated by breakup dynamics to Regime I where coalescence and filament breakup compete. This results in a net decrease in breakup efficiency compared to light rainfall without SFI, and a significant increase in the number concentration of drops >0.7 mm, corresponding to changes in raindrops between 1 and 2 mm by one order of magnitude (e.g., Figure 9e,f). Because the most significant differences in rainfall spectra with and without fog are found for small and intermediate size raindrops, this represents a significant detection challenge to radar measurements (Figure S1b).

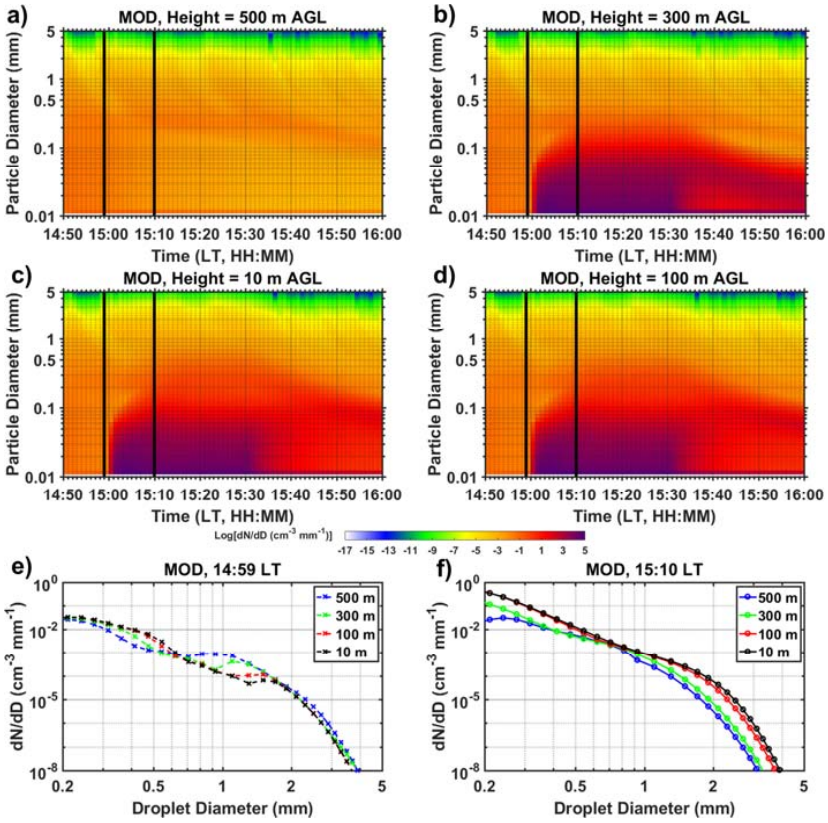

Figure 9. (**Top**) Time series of simulated drop size distributions at four different heights (clockwise: 500-, 300-, 100-, 10-m AGL). The black vertical lines in (**a**–**d**) mark 14:49 LT and 15:10 LT. (**Bottom**) Simulated rain droplet spectra at 14:59 LT (**e**) and 15:10 LT (**f**) at 500-, 300-, 100-, 10-m AGL.

By introducing the local LLCF observations in the model simulations of rainfall on the western slopes, this study adds to previous work in the inner region [16,18] demonstrates the importance of LLCF on modulating the diurnal cycle of orographic precipitation via SFI and illustrated the physical mechanisms of the low-level rainfall amplification due to enhanced coalescence efficiency across the spectrum and change in the breakup mode of larger drops. However, ground-based measurements in mountainous regions are severely lacking and limited by their short sampling duration and small spatial coverage. Over the past two decades, satellite remote sensing is widely utilized to provide a global view of cloud and precipitation distributions and enables long-term monitoring of the Earth's systems, in particular with the advent of active sensors [24]. The vertical enhancement in intermediate raindrop sizes results in moderate reflectivity with nonlinear steeper reflectivity gradients for moderate to heavy rainfall intensities (e.g., ~10 mm/h in the present case study) at low levels and lower elevations as reported by Wilson and Barros [18]. This behavior is compounded with ground-clutter effects of satellite observations in complex terrain that account for the spatial and temporal characteristics in rainfall retrieval errors in the Tropical Rainfall Measurement Mission (TRMM) Precipitation Radar (PR) identified by Duan et al. [14] and Prat and Barros [17]. Next,

multi-satellite observations will be applied to investigate the spatial and temporal variability of LLCF, and their optical and microphysical properties in the SA, aiming at elucidating the role of LLCF in orographic precipitation at the regional scale.

3.2. Satellite-Based Climatology of CBH Using CALIOP and CPR

Previous studies [59,60] have shown that variations in CBHs are correlated to key physical processes in the atmosphere. Changes in CBH directly influence cloud microphysics and optical properties and link to variations in surface fluxes, atmospheric circulation and planetary boundary layer structure. CBH is the most ambiguous cloud property in all available CALIPSO and CloudSat products, especially in complex terrain, and yet is critical to distinguish low-level clouds (LLC) relative to the topography. Over the study region, two daytime CALIOP tracks (indicated by red dotted lines in Figure 1b) overpassing KAVL and KGEV and one nighttime CALIOP track (indicated by blue dotted lines in Figure 1b) overpassing KRHP were analyzed. Due to the battery anomaly on 17 April 2011, only daytime CloudSat data are collected after October 2011. Thus, only daytime CPR observations (ground tracks denoted by orange lines) are employed in this study. CALIOP and CPR fly over the KAVL station around 18:50 UTC (14:50 LT) and the KGEV station around 18:45 UTC (14:45 LT) during the daytime, and the KRHP station around 7:45 UTC (3:45 LT) at night. The ceilometer observations summarized in Figure 4 provide a comprehensive view of the diurnal and seasonal cycles of ground-based observations of LLCF.

3.2.1. Single Sensor Analysis

To assess the strengths and weaknesses of CALIOP and CPR sensors over this region, a direct and independent evaluation of satellite measurements for each sensor against near-simultaneous ground ceilometer observations at the KAVL and KGEV stations for the daytime overpasses was conducted first. As stated earlier, the CALIOP CBH is obtained from the Level 2 cloud layer product at 333-m horizontal resolution, and the CPR CBH is defined as the height of the lowest bin with cloud mask larger than 20 in each profile from the 2B-GEOPROF product. For pixel-to-point comparisons, satellite CBH estimates are matched with ceilometer CBHs at KAVL (KGEV) that are acquired within a 5-min (20-min) window centered over the satellite overpass time and located within the corresponding satellite footprints. Similar comparisons with ceilometer measurements were also conducted with the CALIOP Level 2 cloud layer product at coarser horizontal resolutions (1- and 5-km). To avoid introducing uncertainties of the sampling volume by collocating the CALIOP and CPR, the comparisons were conducted separately at their original pixel resolutions (333-m, 1-km and 5-km for CALIOP, 1.4 km for CPR). It should be noted that the revisit time of CALIPSO/CloudSat overpasses is 16 days, and the ground track of each overpass is not perfectly overlapped. Thus, the time- and space-collocated comparisons between the individual sensor and ceilometers are very limited (<40) for the entire study period (June 2006–October 2016), thus insufficient to render any conclusions with statistical significance (not shown here). Next, the merging method described in Section 2.2 is applied to combine CPR and CALIOP products of 10-year CBH observations, followed by an evaluation of the combined CBH estimates against ground-based ceilometer measurements to demonstrate their performance in detecting LLCF in the SA.

3.2.2. Combined Sensor Analysis

As Lidar signals suffer stronger attenuation than the radar, the detection skill of the CALIOP is highly sensitive to sampling area. Thin scattered clouds are likely to be missed by CALIOP at its highest resolution (333 m $\times$ 70 m), thereby further decreasing the chance of LLCF detection. Thus, the CALIOP data at 333-m was first horizontally averaged and sampling boxes of different sizes were designed with the ground station at the center. Various values of averaging length-scales (i.e., 5-, 10-, 20-, 30-, 40-km) of CALIOP 333-m CBHs were assessed with the 5-min ASOS dataset from the KAVL station for the 10-year study period, as summarized in Table 3. At this site, ceilometer measurements

within a 5-min window centered over the overpass time were used, amounting to 201 comparison pairs between CALIOP and the ceilometer. For the comparisons presented hereafter, simultaneous detections of CBH by the satellite and ceilometer are considered as correct detections; CBH detections by the satellite but not reported by the ceilometer are treated as false alarms (FA); CBH detections by the ceilometer when satellite observations are absent or exceed the upper limit of the ceilometer detection range (3.6 km AGL) are treated as missed detections (MD); CBH detections reported by neither of the satellite and the ceilometer are considered as correct rejections. The detectability statistics indicate the optimal averaging scale of 20 km as it achieves the highest correlation with the in situ measurements (Table 3). This process was repeated for the two other AWOS sites (KGEV and KRHP) as reported in Tables 4 and 5. Note that 20-min ceilometer datasets are available at AWOS sites, thus a 20-min window centered over the overpass time is applied to obtain the matched ceilometer CBHs. This results in total comparison pairs of 211 and 209 for KGEV and KRHP, respectively. The results in Tables 4 and 5 show that the optimal scale is 30 km for both AWOS stations. We can see that the selection of the optimal averaging scale highly depends on the local climatology and available ground data sources (e.g., temporal resolution). Therefore, the optimal sampling size for other regions, especially mountainous areas, can be determined from local ground observations if possible in a manner similar to the methodology applied in this study, or through careful iteration.

Table 3. Contingency tables and correlation coefficients (r) of ceilometer cloud base heights (CBHs) at KAVL and daytime satellite retrieved CBHs using the following products: averaged CALIOP Level 2 cloud layer product (333-m CBHs) at 5-, 10-, 20-, 30-, and 40-km horizontal scale; merged CALIOP-CPR CBHs using 10- and 20-km averaging scales for the CALIOP data, following the method outlined in Figure 2. Values in parentheses are expressed as a percentage of the total number of observation pairs (last column of the table). Note the 5-min window centered over the satellite overpass time is applied to obtain the matched ceilometer CBHs at KAVL.

	Correct Detection	False Alarm	Missed Detection	Correct Rejection	Correlation Coef. (r)	Total # Pairs
CALIOP (5 km)	38 (19%)	2 (1%)	60 (30%)	101 (50%)	0.50	201
CALIOP (10 km)	47 (24%)	2 (1%)	51 (25%)	101 (50%)	0.52	201
CALIOP (20 km)	64 (32%)	9 (4%)	34 (17%)	94 (47%)	0.56	201
CALIOP (30 km)	66 (33%)	15 (7%)	32 (16%)	88 (44%)	0.51	201
CALIOP (40 km)	69 (34%)	21 (11%)	29 (14%)	82 (41%)	0.50	201
Merged (10 km)	70 (35%)	5 (2%)	28 (14%)	98 (49%)	0.61	201
Merged (20 km)	86 (43%)	12 (6%)	12 (6%)	91 (45%)	0.66	201

Table 4. Contingency tables and correlation coefficients (r) of ceilometer CBHs at KGEV and daytime satellite retrieved CBHs using the following products: averaged CALIOP Level 2 cloud layer product (333-m CBHs) at 5-, 10-, 20-, 30-, and 40-km horizontal scale; merged CALIOP-CPR CBHs using 20- and 30-km averaging scales for the CALIOP data, following the method outlined in Figure 2. Values in parentheses are expressed as a percentage of the total number of observation pairs (last column of the table). Note the 20-min window centered over the satellite overpass time is applied to obtain the matched ceilometer CBHs at KGEV.

	Correct Detection	False Alarm	Missed Detection	Correct Rejection	Correlation Coef. (r)	Total # Pairs
CALIOP (5 km)	58 (28%)	4 (2%)	70 (33%)	79 (37%)	0.38	211
CALIOP (10 km)	61 (29%)	6 (3%)	67 (32%)	77 (36%)	0.36	211
CALIOP (20 km)	77 (36%)	6 (3%)	51 (25%)	77 (36%)	0.49	211
CALIOP (30 km)	90 (43%)	12 (6%)	38 (18%)	71 (33%)	0.52	211
CALIOP (40 km)	95 (45%)	18 (9%)	33 (15%)	65 (31%)	0.47	211
Merged (20 km)	100 (47%)	8 (4%)	28 (13%)	75 (36%)	0.59	211
Merged (30 km)	110 (52%)	14 (7%)	18 (8%)	69 (33%)	0.63	211

Table 5. Contingency tables and correlation coefficients (r) of ceilometer CBHs at KRHP and nighttime satellite retrieved CBHs using different horizontal averaging scales (5-, 10-, 20-, 30-, and 40-km) of CALIOP Level 2 cloud layer product (333-m CBHs). Values in parentheses are expressed as a percentage of the total number of observation pairs (last column of the table). Note the 20-min window centered over the satellite overpass time is applied to obtain the matched ceilometer CBHs at KRHP.

	Correct Detection	False Alarm	Missed Detection	Correct Rejection	Correlation Coef. (r)	Total # Pairs
CALIOP (5 km)	41 (20%)	8 (4%)	70 (33%)	90 (43%)	0.22	209
CALIOP (10 km)	44 (21%)	8 (4%)	67 (32%)	90 (43%)	0.32	209
CALIOP (20 km)	63 (30%)	31 (15%)	48 (23%)	67 (32%)	0.38	209
CALIOP (30 km)	76 (36%)	43 (21%)	35 (17%)	55 (26%)	0.47	209
CALIOP (40 km)	77 (37%)	47 (22%)	34 (16%)	51 (25%)	0.43	209

The merging methodology (see the diagram in Figure 2) was applied to combine the CPR data and two resolutions of the CALIOP data at KAVL (10- and 20-km) and KGEV (20- and 30-km) sites, based on the averaging scales examined above. As shown in the last two rows of Tables 3 and 4, the merged estimates during daytime show improved skill over the averaged CALIOP alone. Combining the CPR data and the optimal averaging of CALIOP data at KAVL (20-km, last row of Table 3) and KGEV (30-km, last row of Table 4) sites, respectively, the merged results indicate higher probabilities of correct detections (43% for KAVL and 52% for KGEV), fewer occurrences of MD (6% KAVL and 8% for KGEV), and larger correlation coefficients (0.66 for KAVL and 0.63 for KGEV). It is expected that slightly more FA (6% for KAVL and 7% for KGEV) are resulted in the merged estimates. At nighttime, the merging method is not applicable as no CPR data is recorded after October 2011, and the sample size prior to that date is small. Thus, only the CALIOP measurements were used and averaged for nighttime comparisons at KRHP. As expected, the detectability statistics are not as notable as the merged estimates but the averaging of CALIOP pixels shows clear advantages over the original Level 2 layer products with small sample size. It is important to keep in mind the uncertainties associated with the sampled cloud-volume agreement when averaged ground-based measurements over a certain temporal resolution are directly compared to fast-moving space-based observations, especially at coarse horizontal resolutions and/or different temporal scales [43]. Therefore, the discrepancies between satellite estimates and ground observations may be in part due to large temporal averaging intervals (e.g., 30-min) of the ground ceilometers, which lack representativeness of rapidly changing clouds over mountainous regions. In particular, LLCF typically have short lifetimes and even shorter spatial correlation scales in complex terrain, and there are inherent inconsistencies between the observing strategies used by ceilometers (bottom-up) and satellites (top-down) due to severe attenuation of the latter especially when multilayer clouds are present, which stands as a critical challenge for the validation of satellite products. A close examination of the vertical profiles of radar and Lidar observations for the FA and MD cases reveals distinct observational deficiencies of the merged estimates of CALIOP and CPR. For FA, the error is attributed to large horizontal averaging of Lidar signals under scattered cloudiness conditions. For MD, both sensors are limited in detecting LLCF in the presence of thick upper clouds and/or in unfavorable weather conditions (e.g., mist, rain) due to significant attenuation of CALIOP signals and low sensitivity of the CPR, in addition to ground clutter effects of both sensors.

Even though twice-daily satellite observations (around 3:45 LT and 14:45–14:50 LT) cannot capture the full diurnal range in the SAM, they provide a useful illustration of nighttime-daytime contrasts over the study region. Figure 10 displays the seasonal histograms of satellite CBH estimates (bottom panel) compared to the first layer CBHs detected from the ground ceilometers at the satellite overpass time from June 2006 to October 2016 (top panel). The total number of observation days is denoted in parentheses after each season. Note the merged products (CALIOP-CPR) at KAVL and KGEV sites at daytime are derived from the CPR data and averaged CALIOP data at their corresponding

optimal scales (KAVL: 20-km, KGEV: 30-km) and the nighttime CALIOP data averaged at 30-km horizontal scale are used for comparisons at KRHP site. For daytime cases at KAVL (see Figure 10a,d), the occurrence frequencies of the combined satellite observations, and the ceilometer in summer are in good agreement with both peaking at 1.5–2 km MSL, though CBH values below 1.5 km are still missed by the merged satellite estimates for all seasons. These MDs again point out the limitation of both active sensors in detecting LLCF when surface clutter and low sensitivity to small drops hinder detection by the CPR and the CALIOP signals suffer strong attenuation due to optically thick clouds aloft. At KGEV (see Figure 10b,e), the merged satellite CBHs during daytime capture well the variations in the spring, summer and fall seasons, with distributions peaking at 1.5–2 km, 2–2.5 km, and 1.5–2 km, respectively. Similarly, both satellite sensors missed daytime clouds detected by the ceilometer near the surface (below 1.5 km). At KRHP (see Figure 10c,f), nighttime CALIOP succeeds to detect frequency maxima of LLCF below 1 km in summer and fall, likely associated with nocturnal fog often recorded by the ceilometer in these seasons (see Figure 4f). The superior performance of nighttime CALIOP detections can be explained by that Lidar signals are less noisy during nighttime as compared to daytime observations that are subject to solar radiation contamination in the background [27]. In winter, both satellite and ceilometer distributions peak around 1–1.5 km, however, the maximum in nighttime LLCF occurrences is underestimated by the CALIOP.

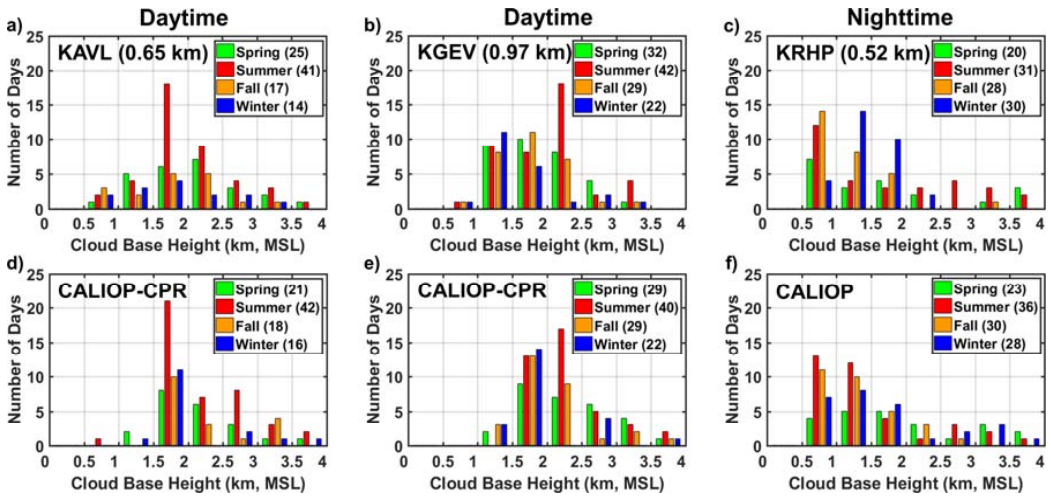

Figure 10. Probability distributions using 10-year (June 2006–October 2016) observations of CBHs from: (**a**) the ground ceilometer at KAVL (elevation: 0.65 km) around daytime overpass (~14:50 LT); (**b**) the ground ceilometer at KGEV (elevation: 0.97 km) around daytime overpass (~14:45 LT); (**c**) the ground ceilometer at KRHP (elevation: 0.52 km) around nighttime overpass (~3:45 LT); (**d**) the merged CALIOP-CPR CBHs for daytime cases at KAVL; (**e**) the merged CALIOP-CPR CBHs for daytime cases at KGEV; (**f**) the averaged CALIOP CBHs at 30-km horizontal scale for nighttime cases at KRHP. Note the total number of observation days is denoted in parentheses after each season (spring: April–June, summer: July–September, fall: October–December, and winter: January–March) and the elevation of each site is denoted in parentheses after its name in (**a**–**c**).

In order to investigate the spatial variability of LLCF along the entire satellite tracks, we define $0.1^\circ \times 0.1^\circ$ (10 km × 10 km) grid boxes over the entire study region. As shown in Figure 1b, three daytime and four nighttime satellite orbits are mapped in this region with overpass times between 14:40–15:10 LT and 3:30–4:00 LT, respectively. For each daytime overpass, the merged CALIOP-CPR CBH retrieval at each grid cell is determined from the CALIOP and CPR observations within the grid box, using the methodology discussed in Section 2.2. For each nighttime overpass, the CBHs from CALIOP 333-m cloud layer products are averaged horizontally within each sampling box following the algorithm from Zhang et al. [44] to derive CALIOP CBH at each grid cell. Figure 11 displays the

spatial distribution of LLCF along CALIPSO/CloudSat tracks over the study region. Here, only grid cells with at least 30 overpasses and satellite observed CBH below 4 km MSL (consistent with the upper detection limit of ground ceilometers) are used to calculate the mean and coefficient of variance (CV) values at each grid cell. Satellite CBHs relative to MSL are converted to AGL. It is apparent that variations in CBH show a pronounced spatial pattern linked to the topography variability (terrain elevation denoted by contour lines: 500 m-solid grey, 1000 m-solid black, and 1500 m-dotted black) in this region. The merged estimates during daytime indicate relatively shallower bases of LLCF persistently observed over the mountainous area than the adjacent plains, as suggested by smaller mean and CV values over high terrain (see Figure 11b). The nighttime CALIOP observations exhibit generally lower cloud bases than daytime CBHs over the SAM, illustrating a more significant contrast of cloud base levels between mountainous regions and lowland area. We can also note that relatively larger variations over time are evident for nighttime retrievals compared to daytime merged estimates (Figure 11 b,d). For comparison, the ceilometer observations at KRHP, KAVL, and KGEV sites (marked by the purple crosses from left to right in Figure 11) around the satellite overpass time are also present. The mean values of ceilometer CBHs (see their histograms in Figure 10a–c) are used to evaluate the corresponding satellite CBH mean at the grid boxes where ground ceilometers are located. The ceilometer CBHs at KAVL (1.4 km AGL) and KGEV (0.9 km AGL) during daytime are overestimated by the merged CBHs by 200 m and 500 m, respectively while the ceilometer CBH at KRHP (0.9 km AGL) during nighttime is slightly underestimated by the CALIOP CBH. The former are located on the Blue Ridge along which persistent shallow clouds and fog banks form on the eastern slope of the SAM (e.g., Black Mountains and Blue Ridge).

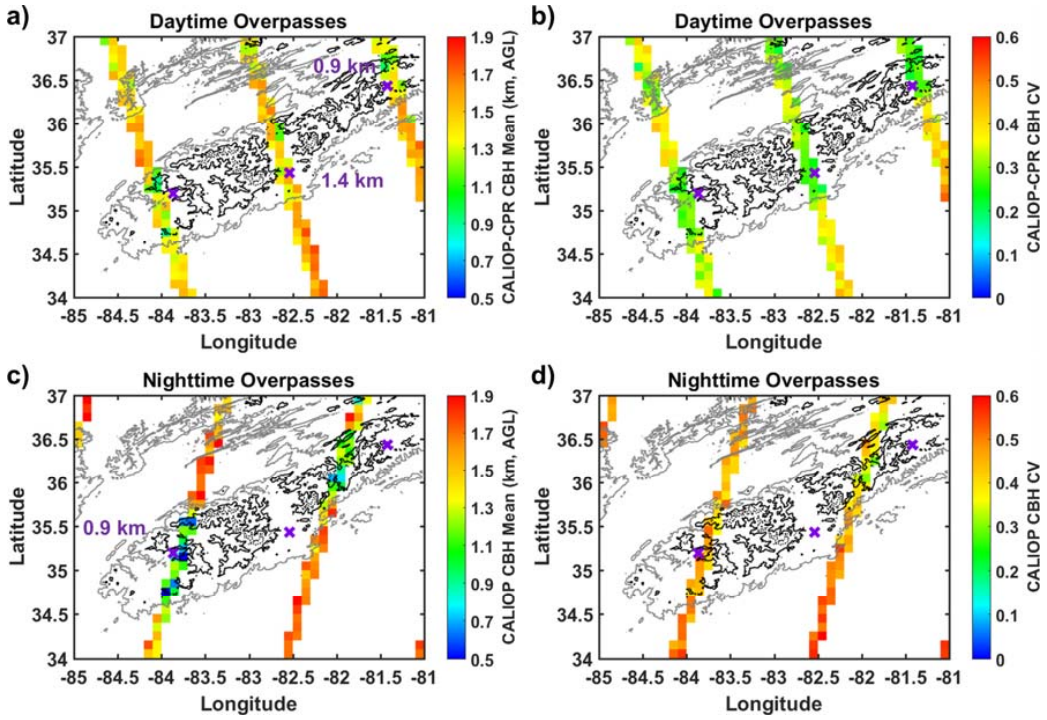

Figure 11. (**Top**) Mean (**a**) of CALIOP-CPR CBHs (km, AGL) for low-level clouds and fog (LLCF, merged CBH < 4 km MSL) and the corresponding coefficient of variance (CV; **b**) in each grid box (0.1° × 0.1°) for daytime overpasses. (**Bottom**) Mean (**c**) of CALIOP CBHs (km, AGL) for LLCF (CALIOP CBH < 4 km MSL) and the corresponding CV (**d**) in each grid box (0.1° × 0.1°) for nighttime overpasses. Contour lines denote terrain elevation of 500 m (solid grey), 1000 m (solid black) and 1500 m (dotted black). Note the three ground ceilometer sites (from left to right: KRHP, KAVL, KGEV) are marked by purple crosses and the numbers next to them represent mean ceilometer CBHs around satellite overpass time.

Overall, the synergy of the combined CALIOP and CPR observations enables us to conduct statistically significant analysis of LLCF over the study region and demonstrates improved detection skills in mapping LLCF over the individual sensor. The daytime results of merged satellite observations are in general agreement with in situ measurements at KAVL and KGEV, especially for the summer season. Nighttime CALIOP observations suffice to capture LLCF below 1 km, in agreement with persistent nocturnal fog observed by the ground ceilometer at KRHP. In the presence of optically thick clouds at upper levels, challenges in detecting daytime shallow boundary clouds with bases lower than 1.5 km still remain for the merged satellite observations, which are attributed to physical limitations of low sensitivity of CPR, strong extinction of CALIOP signals, and ground clutter effects of both sensors. Spatial analysis along satellite tracks illustrates that persistent LLCF are detected over the mountains with relatively lower cloud bases than adjacent plains in the SA, especially during nighttime.

3.3. Satellite-Based Climatology of LLCF Using MODIS

Although CALIOP and CPR demonstrate great potential to resolve the vertical structure of LLCF, previous discussions have also revealed limitations in the application of active sensors over the study region due to long revisit times and narrow satellite swaths. The passive sensor MODIS onboard the Aqua satellite maintains a close formation with CALIPSO and CloudSat satellites. The wide viewing swath of MODIS (2330-km cross-track) can extend the spatial coverage beyond narrow swaths of active sensors and compensate for the sparse temporal sampling that is inadequate to reflect spatial variations in seasonal cycles. The revisit frequency of MODIS over this study region is about one to two days because of its wide viewing swath. Next MODIS observations will be explored to characterize the top, optical, and microphysical properties of LLCF over the SA.

3.3.1. Spatial Patterns of LLCF CTH

MODIS provides high-spectral resolutions of cloud properties at 1-km resolution and significant refinements in its retrieval algorithm are implemented in C6 by evaluating against near-coincident cloud-top observations from the CALIOP [37]. Figure 12 shows the density-colored scatterplots of MODIS CTH at 1-km pixel and the collocated CALIOP CTH for daytime and nighttime observations over the study region. The CALIOP CTH is calculated as the average of CALIOP 333-m CTHs within the MODIS 1-km footprint. There are approximately 3 Lidar profiles within the 1-km field-of-view (FOV) of MODIS. Due to the narrow beam width (~70 m) of CALIOP, only a small fraction of the entire MODIS FOV (1-km) at the Earth's surface is sampled by CALIOP. Thus, uncertainties resulted from the differences in sampling area between MODIS and CALIOP should be kept in mind when interpreting the comparison of their collocated CTH measurements. The viewing angles for all the MODIS pixels in comparison are in the range of 13.6°–16.9°, as the nadir-viewing track of Aqua does not follow the CALIPSO flight track. This results in a parallax effect on the CTH dependence of the collocation [61], which are not taken into account in this study. For daytime cases, we only consider single layer clouds, as determined by the cloud multilayer flag in MODIS. As indicated in Figure 12a, MODIS CTHs agree well with CALIOP CTHs, in particular for low clouds with tops <5 km. This is likely attributed to the new lapse-rate approach applied in C6 to retrieve MODIS CTH of low clouds [61]. The underestimation of daytime CTHs by MODIS is likely associated with its lower sensitivity to small droplets near the cloud top as compared to CALIOP, which is superior in detecting tenuous and geometrically thin clouds. With multi-layer profiles included during nighttime, a systematic high CTH bias of 0.2–1.2 km is found in the MODIS results (Figure 12b). The overestimation by MODIS could be explained by the possible ambiguities induced by its viewing geometry as a longer path through the atmosphere is observed by MODIS at an angle than CALIOP with only nadir view. Overall, the cloud-top product from MODIS demonstrates consistent detections of low clouds (CTH <5 km MSL) with near-simultaneous measurements from CALIOP.

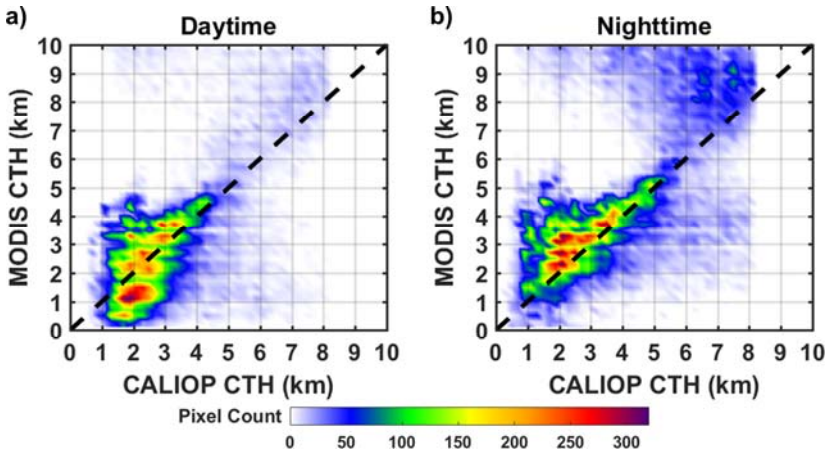

Figure 12. Density-colored scatterplots of MODIS cloud top heights (CTHs) at 1-km pixel and the collocated CALIOP CTHs for daytime (**a**), single-layer clouds only and nighttime (**b**) observations. The dashed black line represents the 1:1 line.

To further probe LLCF distributions using MODIS observations, grid cells of 0.05° × 0.05° (5 km × 5 km) are defined over the entire study region (map in Figure 1b). For each season, the spatial variability of LLCF (CTH < 5 km MSL) observed by MODIS for daytime (~14:00–15:30 LT) and nighttime (~3:00–4:30 LT) overpasses during the 10-year study period are exhibited in Figures 13 and 14, respectively. If there are at least 5 pixels (1-km) with MODIS CTH <5 km within the grid cell, one day is counted in this cell. Only single-layer clouds are considered for daytime overpasses. Inspection of Figure 13 reveals more frequent daytime low-clouds are evident in the warm season (spring and summer) as compared to the cold season (fall and winter). In particular, mountain ridges experience persistent cover of low clouds at daytime in spring and summer. Note that LLCF occurrences in summer are over 50 days/year over the mountains at elevations above 1500 m MSL (dotted black contour lines in Figure 13b). One interesting feature of the LLCF distributions for the warm season is that relatively fewer clouds form above large lakes or artificial reservoirs (indicated by the white dots based on 30-arcsec gridded data from the USDA-NRCS State Soil Geographic Database) impounded by major dams in this region while higher frequencies of cloud occurrences are found over the adjacent lands (Figure 13a,b). Specifically, note the organization of cloudiness between major lakes part of the Tennessee Valley Association (TVA) system of dams to the west of the SAM and away from the large dams in the upper Savannah and Catawba-Pee Dee rivers in the east, which are indicative of the robust role of lake breeze circulations in the organization of LLC formed along southerly and easterly low level moisture convergence patterns [54]. To be specific, the lake breeze refers to thermally driven winds blowing from a large body of open water toward the surrounding lands due to the pressure gradient of the air over the water (high pressure) and dry land (low pressure) produced by differences in their heat capacities during daylight with solar heating. The moisture supply from open water evaporation transported to adjacent lands creates favorable conditions for cloud formation, and even trigger thunderstorms when the atmosphere is unstable in the warm season. By contrast, synoptic winds from west-northwest dominate in the fall and winter, leading to extensive formation of low clouds on the windward side of the SAM. Due to the mountain barrier effect, forced orographic lifting of incoming air masses results in enhanced formation of low-level orographic clouds along the windward slopes but significantly reduced occurrences of low clouds on the leeward side [62,63]. Further, the lake breeze flow is hindered in the cold season as the required pressure gradient is unlikely to form under strong regional winds.

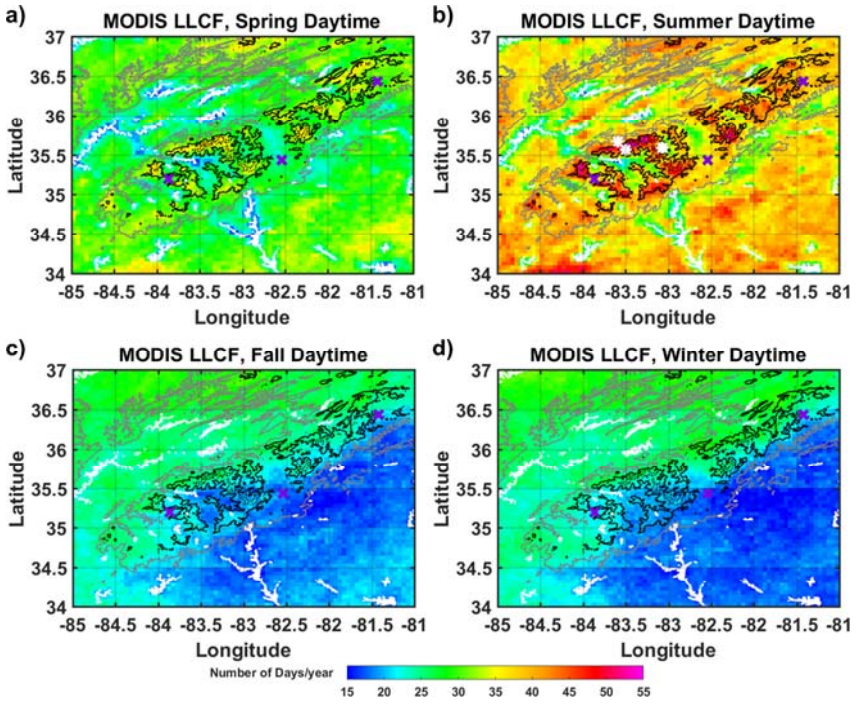

Figure 13. Spatial distributions of MODIS LLCF (CTH <5 MSL, single-layer clouds only) occurrences in each grid box (0.05° × 0.05°) during daytime overpasses for each season (spring: April–June; (**a**) summer: July–September; (**b**) fall: October–December; (**c**) and winter: January–March; (**d**) Contour lines mark terrain elevation of 500 m (solid grey), 1000 m (solid black) and 1500 m (dotted black) and water surface is delineated by white dots. Note the three ground ceilometer sites (from left to right: KRHP, KAVL, and KGEV) are marked by purple crosses and white asterisks in (**b**) denote the four ground fog collectors (from left to right: ELK, CD, PK, and PKT).

Figure 14 displays the seasonal spatial distribution of nighttime LLCF observed by MODIS. As information from visible wavelength is not available at night, we only consider clouds with the confidence level of "confident cloudy" as determined by the cloud mask product (MYD35). In the spring and summer season, high frequencies of nocturnal LLCF occurrences are present in the mountain valleys consistent with regional-scale stability at low levels resulting in the pooling of cold moist air in the inner SAM [54]. At nighttime, this region experiences the highest frequency of LLCF coverage in the winter season compared to other seasons, especially along the windward slopes of the SAM, consistent with forced orographic lifting of westerly and northwesterly winds as noted above. Due to the inherent dependence of cloud properties on viewing geometry, care should be taken when using MODIS products observed over a wide range of sensor zenith angles [64]. Additional spatial distributions of MODIS pixel counts with viewing angles less than 20° for each season during the 10-year study period are provided in Figures S2 and S3. These maps highlight the areas in the study domain with larger fraction of near-nadir observations, which are less prone to the sensor zenith angle biases and likely lends credence to the corresponding observational findings of LLCF detection.

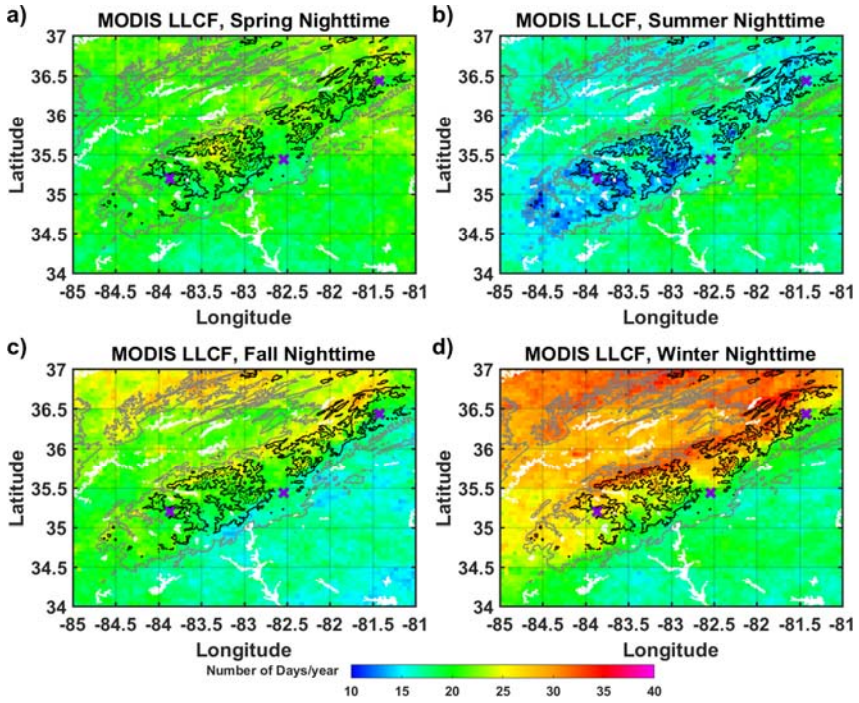

Figure 14. Spatial distributions of MODIS LLCF (CTH <5 MSL, confident cloudy only) occurrences in each grid box (0.05° × 0.05°) during nighttime overpasses in each season (spring: April–June; (**a**) summer: July–September; (**b**) fall: October–December; (**c**) and winter: January–March; (**d**) Contour lines mark terrain elevation of 500 m (solid grey), 1000 m (solid black) and 1500 m (dotted black) and water surface is delineated by white dots. Note the three ground ceilometer sites (from left to right: KRHP, KAVL, and KGEV) are marked by purple crosses.

3.3.2. Optical and Microphysical Properties of LLCF

Next, we focus on characterizing the climatology of optical and microphysical properties of daytime LLCF using the MODIS observations and ground ceilometer measurements. During June 2006–October 2016, the optical and microphysical properties retrieved from MODIS combined with the CBH information obtained from ground ceilometers are utilized to evaluate LLCF properties at these ceilometer sites during daytime overpasses. The analysis is limited to low clouds with top heights less than 5 km MSL when single layer is detected by MODIS. Figure 15 shows the fractional occurrence density maps of collocated MODIS top, optical, and microphysical properties as a function of ceilometer CBHs (AGL) at KRHP, KAVL, and KGEV sites. The ceilometer CBHs are obtained within 5 (20) min of the MODIS overpass time at KAVL (KRHP and KGEV) and are matched with the MODIS pixel within its footprint (1 km). This corresponds to 194 observation pairs at KRHP, 206 pairs at KAVL, and 253 pairs at KGEV for the 10-year study period. LLCF with lower CBHs are more frequent observed at the ridge site (KGEV) compared to the two valley sites (KRHP and KAVL), which is consistent with the previous analysis of 10-year ceilometer observations (Figure 4) and combined CBHs from CALIOP and CPR (Figure 11). Conditional on ground ceilometer detections from bottom-up, the distributions of CWP-CBH and COT-CBH indicate frequent LLCF occurrences at these sites (CBH < 2 km AGL for KRHP and KAVL, CBH < 1.5 km AGL for KGEV), which are associated with small values of vertically integrated cloud properties (CWP < 100 g/m^2 and COT < 15). Although CER exhibits large variability, similarities can be found in the lower-left corner of the diagrams showing a prominent feature of LLCF composed of small liquid water droplets with effective radius around 5–15 μm near cloud tops. Figure 5b shows the ground-based MPS observations of LLCF immersion in the absence of rainfall with CER values around 25 μm in the early morning until 11:00 LT. After 11:00 LT, surface CER values (50–150 μm) are significantly higher than the MODIS CER estimates (5–15 μm) near cloud

tops by a factor of 3–10 because the number of drizzle sized drops increases relative to the LLCF sized drops (<100 μm) that is one to two orders of magnitude lower at mid-day (Figure 5a). This indicates there is significant vertical stratification of the microstructure of LLCF from cloud top to the ground surface, suggesting DSD evolution in the LLCF column proper, thus conditioning the environment for enhanced SFI when the "seeder" light rainfall arrives in the afternoon.

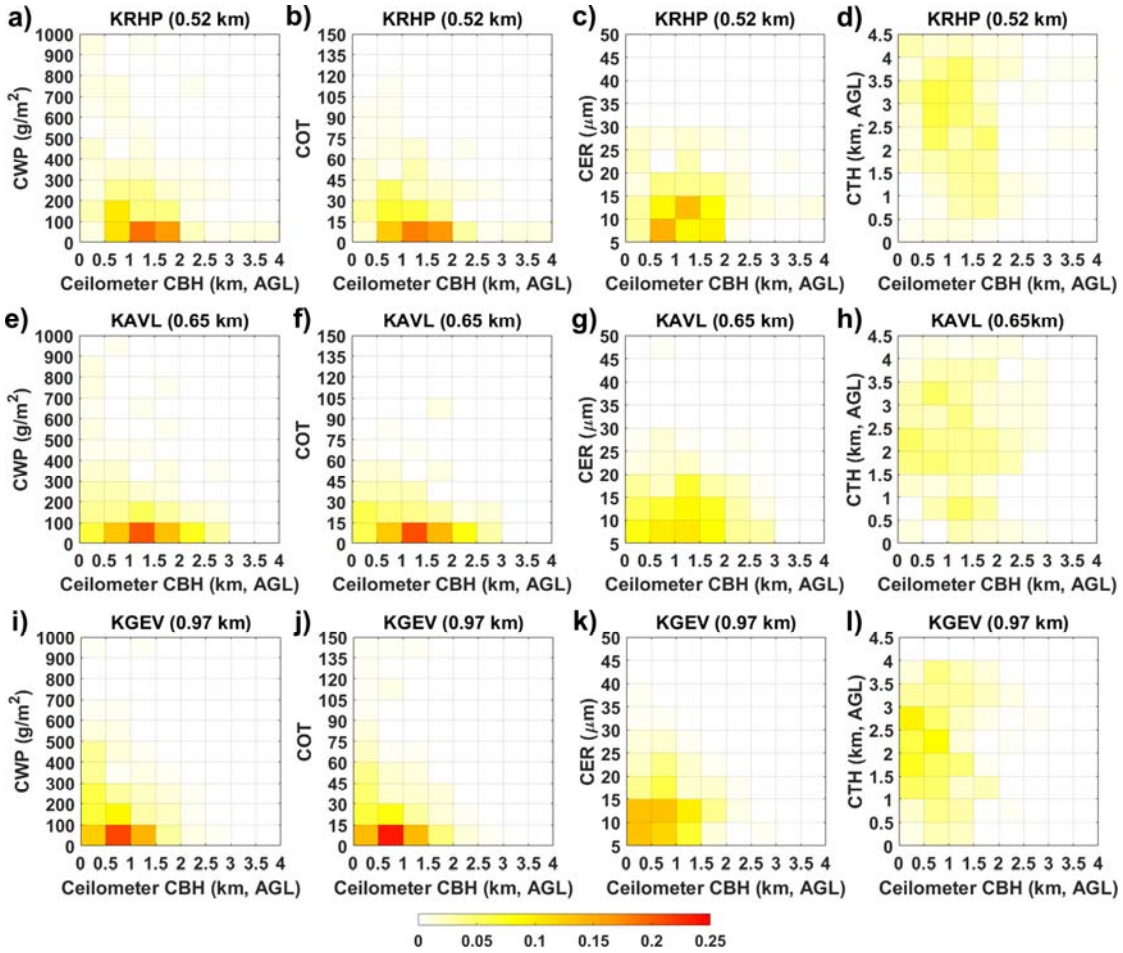

Figure 15. Fractional occurrences of collocated MODIS cloud properties of LLCF (single-layer clouds with CTH < 5 km MSL) as a function of ceilometer CBHs at KRHP (**a**–**d**), KAVL (**e**–**h**), and KGEV (**i**–**l**) during June 2006–October 2016 (daytime overpasses only). Note the elevation of each site is denoted in parentheses after its name. In each panel, CWP represents cloud water path, COT represents cloud optical thickness, and CER represents cloud particle effective radius.

Similar analyses were conducted for 10-year MODIS observations sampled around the ground sites with fog collectors (see Table 1). Within the grid box (5 km × 5 km, as defined in Section 3.3.1) where each ground station is located, Figures S4–S7 present the joint frequency histograms of MODIS CTH and the optical and microphysical properties (CWP, COT, and CER) for each season. Note that only single-layered LLCF measurements with tops below 5 km MSL and near-nadir viewing angles (<20°) are considered in the analysis. As PK and PKT are located at the same grid box, only results for PK are shown here. The system of reference for the MODIS CTHs was converted from MSL to AGL. In the warm season (spring and summer), it is evident that more clouds with lower tops are present over higher elevation sites (CD and PK & PKT) as compared to the valley station (ELK). Regardless of differences in terrain elevation, similar ranges of CWP (~0–200 g/m^2) and COT (0–30) values are observed for LLCF at all ground locations in the warm season (Figures S4 and S5) while larger CWP

and COT values are found in the cold season (Figures S6 and S7). Interestingly, despite low CWP and COT in summer, the corresponding CER values are higher on average and exhibit higher variability (right panel in Figure S5) compared against narrow distributions of low CER values (~5–15 μm) in spring, fall, and winter (right panels in Figures S4, S6, and S7).

4. Discussion

Remote sensing observations of orographic precipitation exhibit large underestimation errors from sub-daily to annual scales tied to landform and topographic complexity generally e.g., [e.g.,1,14,16,53]. In the SAM, which are representative of middle mountains in the tropics and mid-latitudes that are hosts to high biodiversity cloud forests and generally humid ecosystems, nearly a decade of ground-based rainfall accumulation and rainfall microphysics, show that the diurnal cycle of rainfall exhibits an all-season mid-day peak that explains a large fraction of the regional annual freshwater input, and it is critical to regional drought resilience [15,54]. Over roughly the last decade, independent field observations of vertical structure of rainfall, rainfall microphysics, and rainfall intensity and accumulation in the SAM show evidence of low-level enhancement of R-DSDs with rainfall intensities up to one order of magnitude and rainfall accumulations on the order of 200–300% at daily, seasonal and annual time-scales [15,18,58]. These observations are indicative of space-time distributions of rainfall that do not fit the classical orographic precipitation model with strong upslope enhancement characteristic of high-mountain ranges, consistent with the lack of a rain-shadow region in the SE US.

The modeling results in this study evaluated the role of SFI in surface precipitation enhancement around mid-day in the SAM. However, the dynamic evolution of fog microphysics and fog intermittency are not available in the study region and are not represented in the current model. Future research efforts will focus on incorporating enhanced turbulent collision rate to the collision-coalescence process [57] in the column model as well as exploring other contributing physical processes including integration with Large-Eddy Simulations (LES) to better represent winds fields. To derive R-DSDs for the initial and top boundary conditions of the column model simulations, the intercept parameter (N_0) in the negative exponential distribution was assumed based on the MRR reflectively values and the shape parameter were fitted through iteration with a tolerance error of 0.001%. Generally, because the R-DSD is specified at the top of the column, rainfall enhancement by SFI ranges from 3–10 fold, it is not expected that the propagation of uncertainties in the top boundary condition will exceed the uncertainty in rainfall measurements proper. However, because of the importance of large drop sizes in the radar equation, and to understand how SFI modifies precipitation structure for different types of rainfall, the next step is to characterize the propagation uncertainties associated with the fitted intercept and slope parameters on the simulated precipitation evolution. The combination of models and observations can lead toward physically-based representation of LLCF and SFI in remote-sensing retrieval algorithms. Further observations and modeling studies are needed to achieve a comprehensive synthesis for global scale applications.

5. Conclusions

The objective of this study is to understand the physical basis of the observed mid-day peak in rainfall that is also observed in humid mountain regions rich in biodiversity elsewhere (e.g., Central Andes [1]) from local to regional scales and from case-study to climate time-scales. Following Wilson and Barros [18] and Angulo-Martínez and Barros [58] who demonstrated the impact of SFI in amplifying rainfall over the inner mountain region, here the investigation was extended to the western slopes of the SAM using in situ observations and modeling. First, a rainfall column microphysics model constrained by fog observations was used to investigate how SFI modify the R-DSD to reveal that fast SFI (2–5 min time-scales) modify the R-DSD by increasing coalescence efficiency in the small drop range (<0.7 mm diameter), whereas competition between coalescence and breakup dominates for larger drop (3–5 mm diameter). Detailed analysis of the collision dynamics reveals that the presence of high number concentrations of small drops in LLCF changes the collision dynamics of breakup to the

filament-only mode, which results in the balance of coalescence and breakup effects for large drops. The net result is a large increase in the number concentrations of intermediate size raindrops in the 0.7–3 mm range and up to a ten-fold increase in rainfall intensity, with very large changes in the number concentrations between 1–2 mm and up to 3 mm. Second, the focus turned to satellite observations with an eye in building evidence of the role of LLCF in modulating the observed space-time diurnal cycle of precipitation at the regional scale. A 10-year climatology of LLCF habits was developed based on combined CBH estimates from CALIOP and CPR, and on MODIS observations of CTHs, as well as cloud properties including LWP, COT, and cloud-top CER. The climatology shows high-frequency daytime LLCF over mountain ridges in the warm season (especially in summer) shifts to river valleys at nighttime, consistent with previous modeling studies of regional patterns of warm season moisture convergence. In fall and winter, the spatial patterns of LLCF define a cloud-shadow region to the east of the continental divide in the SAM, consistent with cold-season weather patterns. Optical and microphysical properties of LLCF from collocated MODIS and ground ceilometers observations indicate small values of vertically integrated CWP (<100 g/m^2), COT (<15), and CER (<15 μm) at cloud top that increases up to 150 μm near the surface at mid-day before rainfall onset based on the observations. The significant vertical stratification of LLCF microphysics and SFI pose a challenge to satellite-based remote sensing of precipitation in mountainous regions. Further, despite high rainfall rates and LWC, this study shows that, the underestimation of low-level enhancement of precipitation induced by the SFI has a physical basis that is explained by collision dynamics with dominant preference for filament breakup when large numbers of small drops are present, in contrast with microphysics of similar rainfall rates under different rainfall regimes (e.g., deep convection, Figure S1). Thus, the microphysics of SFI pose a critical challenge to radar detection which is further complicated in mountainous regions by ground clutter artifacts [14].

Supplementary Materials: The following are available online at http://www.mdpi.com/2072-4292/9/9/920/s1. Figure S1: (**a**) Regimes of drop collisions delineated according to DE_1 and DE_2: I-Coalescence and Filament Breakup dominate; II-Breakup dominates; III-Drops collide and bounce. Note SE is the surface tension energy neglecting viscosity, CKE is the collision kinetic energy, p is the diameter ratio between the small and larger diameters of two colliding hydrometeors, and We is the Weber number. This figure is adapted from Testik et al. [52]. For details see Testik [65], Testik et al. [52], Prat et al. [21]; (**b**) Conceptual synthesis of seeder-feeder interactions (SFI) impacts on rain drop size distribution (R-DSD) vis-à-vis convective rainfall of the same intensity with respect to a reference light stratiform rainfall; Figure S2: Spatial distributions of MODIS pixel counts with viewing angle less than 20° in each season (spring: April–June, summer: July–September, fall: October–December, and winter: January–March) during daytime overpasses of June 2006–October 2016. Note the three ground ceilometer sites (from left to right: KRHP, KAVL, and KGEV) are marked by purple crosses; Figure S3: Spatial distributions of MODIS pixel counts with viewing angle less than 20° in each season (spring: April–June, summer: July–September, fall: October–December, and winter: January–March) during nighttime overpasses of June 2006–October 2016. Note the three ground ceilometer sites (from left to right: KRHP, KAVL, and KGEV) are marked by purple crosses; Figure S4: Fractional occurrences of MODIS optical and microphysical properties (CWP, COT, and CER) for single-layered LLCF (CTH < 5 km MSL and viewing angle < 20°) as a function of MODIS CTH (AGL) observed in the grid box (0.05° × 0.05°) where each fog collector is located (ELK: **a**–**c**, PK: **d**–**f**, and CD: **g**–**i**) during the spring of June 2006–October 2016 (daytime overpasses only). Note the elevation of each site is denoted in parentheses after its name; Figure S5: Fractional occurrences of MODIS optical and microphysical properties (CWP, COT, and CER) for single-layered LLCF (CTH < 5 km MSL and viewing angle < 20°) as a function of MODIS CTH (AGL) observed in the grid box (0.05° × 0.05°) where each fog collector is located (ELK: **a**–**c**, PK: **d**–**f**, and CD: **g**–**i**) during the summer of June 2006–October 2016 (daytime overpasses only). Note the elevation of each site is denoted in parentheses after its name; Figure S6: Fractional occurrences of MODIS optical and microphysical properties (CWP, COT, and CER) for single-layered LLCF (CTH < 5 km MSL and viewing angle < 20°) as a function of MODIS CTH (AGL) observed in the grid box (0.05° × 0.05°) where each fog collector is located (ELK: **a**–**c**, PK: **d**–**f**, and CD: **g**–**i**) during the fall of June 2006–October 2016 (daytime overpasses only). Note the elevation of each site is denoted in parentheses after its name; Figure S7: Fractional occurrences of MODIS optical and microphysical properties (CWP, COT, and CER) for single-layered LLCF (CTH < 5 km MSL and viewing angle < 20°) as a function of MODIS CTH (AGL) observed in the grid box (0.05° × 0.05°) where each fog collector is located (ELK: **a**–**c**, PK: **d**–**f**, and CD: **g**–**i**) during the winter of June 2006–October 2016 (daytime overpasses only). Note the elevation of each site is denoted in parentheses after its name.

Acknowledgments: This research was funded in part by NASA grant NNX13AH39G and NNX16AM28G to the second author. The authors thank Anna M. Wilson and graduate student Malarvizhi Arulraj for the deployment and maintenance of fog collectors and Duke's H2F (Haze to Fog) mobility facility (including the MPS, fog gauge, raingauge, and WXT).

Author Contributions: The first author conducted the satellite data analysis and ran the microphysical model simulations. Both authors contributed to the research design, analysis, and interpretation of results and writing of the manuscript.

Conflicts of Interest: The authors declare no conflict of interest.

Abbreviations

AGL	Above Ground Level
ASOS	Automated Surface Observing System
ATBDs	Algorithm Theoretical Basis Documents
AWOS	Automated Weather Observing System
C6	Collection 6
CALIOP	Cloud-Aerosol Lidar with Orthogonal Polarization
CALIPSO	Cloud-Aerosol Lidar and Infrared Pathfinder Satellite Observations
CBH	Cloud Base Height
CD	Clingmans Dome
CER	Cloud Particle Effective Radius
COT	Cloud Optical Thickness
CPR	Cloud Profiling Radar
CTH	Cloud Top Height
CTP	Cloud Top Pressure
CV	Coefficient of Variance
CWP	Cloud Water Path
ELK	Elkmont
EOS	Earth Observing System
FA	False Alarms
FAA	Federal Aviation Administration
F-DSDs	Fog Drop Size Distributions
FOV	Field-Of-View
GEOPROF	Geometrical Profiling Product
LES	Large-Eddy Simulations
LLC	Low-Level Clouds
LLCF	Low-Level Clouds and Fog
LWC	Liquid Water Content
MD	Missed Detections
MODIS	Moderate Resolution Imaging Spectroradiometer
MPS	Meteorological Particle Spectrometer
MRR	Micro Rain Radar
MSL	Mean Sea Level
NCDC	National Climatic Data left
NOAA	National Oceanic and Atmospheric Administration
PK	Purchase Knob
PKT	Purchase Knob Tower
PR	Precipitation Radar
R-DSDs	Rain Drop Size Distributions
RG	Rain Gauge
SA	Southern Appalachians
SAM	Southern Appalachian Mountains
SBE	Stochastic Break Equation
SCE	Stochastic Collection Equation
SFI	Seeder-Feeder Interactions
SM	Statute Miles
TBC	Top Boundary Condition
TRMM	Tropical Rainfall Measurement Mission
TVA	Tennessee Valley Association

Appendix A. Additional Formulae

The droplet effective radius (r_e) is calculated as

$$r_e = \frac{\sum_{i=1}^{bins} r_i^3 n_i}{\sum_{i=1}^{bins} r_i^2 n_i} \tag{A1}$$

The liquid water content (*LWC*) is computed as

$$LWC = \frac{4\pi}{3}\rho_w \sum_{i=1}^{bins} n_i r_i^3 \tag{A2}$$

where *ni* is the number concentration of droplet in the *i*th bin ($i = 1, 2, \ldots, bins$) and *ri* is the radius of droplet in the *i*th bin. In Equation (A2), ρ_w is the density of water.

References

1. Barros, A.P. Orographic precipitation, freshwater resources, and climate vulnerabilities in mountainous regions. In *Climate Vulnerability: Understanding and Addressing Threats to Essential Resources*; Elsevier: Amsterdam, The Netherlands, 2013; pp. 57–78.
2. Gultepe, I.; Tardif, R.; Michaelides, S.C.; Cermak, J.; Bott, A.; Bendix, J.; Müller, M.D.; Pagowski, M.; Hansen, B.; Ellrod, G.; et al. Fog research: A review of past achievements and future perspectives. *Pure Appl. Geophys.* **2007**, *164*, 1121–1159. [CrossRef]
3. Bruijnzeel, L.A. Hydrological functions of tropical forests: Not seeing the soil for the trees? *Agric. Ecosyst. Environ.* **2004**, *104*, 185–228. [CrossRef]
4. Goldsmith, G.R.; Matzke, N.J.; Dawson, T.E. The incidence and implications of clouds for cloud forest plant water relations. *Ecol. Lett.* **2013**, *16*, 307–314. [CrossRef] [PubMed]
5. Gotsch, S.G.; Crausbay, S.D.; Giambelluca, T.W.; Weintraub, A.E.; Longman, R.J.; Asbjornsen, H.; Hotchkiss, S.C.; Dawson, T.E. Water relations and microclimate around the upper limit of a cloud forest in maui, hawai'i. *Tree Physiol.* **2014**, *34*, 766–777. [CrossRef] [PubMed]
6. Oliveira, R.S.; Eller, C.B.; Bittencourt, P.R.; Mulligan, M. The hydroclimatic and ecophysiological basis of cloud forest distributions under current and projected climates. *Ann. Bot.* **2014**, *113*, 909–920. [CrossRef] [PubMed]
7. Weathers, K.C. The importance of cloud and fog in the maintenance of ecosystems. *Trends Ecol. Evol.* **1999**, *14*, 214–215. [CrossRef]
8. National Climatic Data Center. *Climate Atlas of the United States*; U.S. Dept. of Commerce, National Oceanic and Atmospheric Administration: Ashville, NC, USA, 2000.
9. Berry, Z.C.; Smith, W.K. Cloud pattern and water relations in picea rubens and abies fraseri, southern Appalachian mountains, USA. *Agric. For. Meteorol.* **2012**, *162*, 27–34. [CrossRef]
10. Berry, Z.C.; Hughes, N.M.; Smith, W.K. Cloud immersion: An important water source for spruce and fir saplings in the southern Appalachian mountains. *Oecologia* **2014**, *174*, 319–326. [CrossRef] [PubMed]
11. Berry, Z.C.; Smith, W.K. Ecophysiological importance of cloud immersion in a relic spruce-fir forest at elevational limits, southern Appalachian mountains, USA. *Oecologia* **2013**, *173*, 637–648. [CrossRef] [PubMed]
12. Johnson, D.M.; Smith, W.K. Low clouds and cloud immersion enhance photosynthesis in understory species of a southern Appalachian spruce–fir forest (USA). *Am. J. Bot.* **2006**, *93*, 1625–1632. [CrossRef] [PubMed]
13. Barros, A.P.; Lettenmaier, D.P. Dynamic modeling of the spatial distribution of precipitation in remote mountainous areas. *Mon. Weather Rev.* **1993**, *121*, 1195–1214. [CrossRef]
14. Duan, Y.; Wilson, A.M.; Barros, A.P. Scoping a field experiment: Error diagnostics of trmm precipitation radar estimates in complex terrain as a basis for iphex2014. *Hydrol. Earth Syst. Sci.* **2015**, *19*, 1501–1520. [CrossRef]
15. Wilson, A.M.; Barros, A.P. Landform controls on low level moisture convergence and the diurnal cycle of warm season orographic rainfall in the southern appalachians. *J. Hydrol.* **2015**, *531*, 475–493. [CrossRef]
16. Prat, O.P.; Barros, A.P. Ground observations to characterize the spatial gradients and vertical structure of orographic precipitation—Experiments in the inner region of the Great Smoky mountains. *J. Hydrol.* **2010**, *391*, 141–156. [CrossRef]

17. Prat, O.P.; Barros, A.P. Assessing satellite-based precipitation estimates in the Southern Appalachian mountains using rain gauges and TRMM PR. *Adv. Geosci.* **2010**, *25*, 143–153. [CrossRef]
18. Wilson, A.M.; Barros, A.P. An investigation of warm rainfall microphysics in the Southern Appalachians: Orographic enhancement via low-level seeder–feeder interactions. *J. Atmos. Sci.* **2014**, *71*, 1783–1805. [CrossRef]
19. Prat, O.P.; Barros, A.P. A robust numerical solution of the stochastic collection–breakup equation for warm rain. *J. Appl. Meteorol. Climatol.* **2007**, *46*, 1480–1497. [CrossRef]
20. Prat, O.P.; Barros, A.P. Exploring the use of a column model for the characterization of microphysical processes in warm rain: Results from a homogeneous rainshaft model. *Adv. Geosci.* **2007**, *10*, 145–152. [CrossRef]
21. Prat, O.P.; Barros, A.P.; Testik, F.Y. On the influence of raindrop collision outcomes on equilibrium drop size distributions. *J. Atmos. Sci.* **2012**, *69*, 1534–1546. [CrossRef]
22. Chen, R.; Chang, F.-L.; Li, Z.; Ferraro, R.; Weng, F. Impact of the vertical variation of cloud droplet size on the estimation of cloud liquid water path and rain detection. *J. Atmos. Sci.* **2007**, *64*, 3843–3853. [CrossRef]
23. Hagihara, Y.; Okamoto, H.; Yoshida, R. Development of a combined CloudSat-CALIPSO cloud mask to show global cloud distribution. *J. Geophys. Res.* **2010**, *115*, D00H33. [CrossRef]
24. Stephens, G.L.; Vane, D.G.; Boain, R.J.; Mace, G.G.; Sassen, K.; Wang, Z.; Illingworth, A.J.; O'Connor, E.J.; Rossow, W.B.; Durden, S.L.; et al. The CloudSat mission and the a-train: A new dimension of space-based observations of clouds and precipitation. *Bull. Am. Meteorol. Soc.* **2002**, *83*, 1771–1790. [CrossRef]
25. Winker, D.M.; Hunt, W.H.; McGill, M.J. Initial performance assessment of CALIOP. *Geophys. Res. Lett.* **2007**, *34*, L19803. [CrossRef]
26. Mace, G.G.; Zhang, Q.; Vaughan, M.; Marchand, R.; Stephens, G.; Trepte, C.; Winker, D. A description of hydrometeor layer occurrence statistics derived from the first year of merged CloudSat and CALIPSO data. *J. Geophys. Res.* **2009**, *114*, D00A26. [CrossRef]
27. Young, S.A.; Vaughan, M.A. The retrieval of profiles of particulate extinction from cloud-aerosol lidar infrared pathfinder satellite observations (CALIPSO) data: Algorithm description. *J. Atmos. Ocean. Technol.* **2009**, *26*, 1105–1119. [CrossRef]
28. Winker, D.M.; Vaughan, M.A.; Omar, A.; Hu, Y.; Powell, K.A.; Liu, Z.; Hunt, W.H.; Young, S.A. Overview of the CALIPSO mission and CALIOP data processing algorithms. *J. Atmos. Ocean. Technol.* **2009**, *26*, 2310–2323. [CrossRef]
29. Winker, D.M.; Pelon, J.R.; McCormick, M.P. The CALIPSO mission: Spaceborne lidar for observation of aerosols and clouds. *Proc. SPIE* **2003**. [CrossRef]
30. Vaughan, M.A.; Powell, K.A.; Winker, D.M.; Hostetler, C.A.; Kuehn, R.E.; Hunt, W.H.; Getzewich, B.J.; Young, S.A.; Liu, Z.; McGill, M.J. Fully automated detection of cloud and aerosol layers in the CALIPSO lidar measurements. *J. Atmos. Ocean. Technol.* **2009**, *26*, 2034–2050. [CrossRef]
31. Stephens, G.L.; Vane, D.G.; Tanelli, S.; Im, E.; Durden, S.; Rokey, M.; Reinke, D.; Partain, P.; Mace, G.G.; Austin, R.; et al. CloudSat mission: Performance and early science after the first year of operation. *J. Geophys. Res.* **2008**, *113*, D00A18. [CrossRef]
32. Marchand, R.; Mace, G.G.; Ackerman, T.; Stephens, G. Hydrometeor detection using CloudSat—An earth-orbiting 94-Ghz cloud radar. *J. Atmos. Ocean. Technol.* **2008**, *25*, 519–533. [CrossRef]
33. Mace, G.G.; Zhang, Q. The cloudsat radar-lidar geometrical profile product (RL-GeoProf): Updates, improvements, and selected results. *J. Geophys. Res. Atmos.* **2014**, *119*, 9441–9462. [CrossRef]
34. Ackerman, S.A.; Strabala, K.I.; Menzel, W.P.; Frey, R.A.; Moeller, C.C.; Gumley, L.E. Discriminating clear sky from clouds with MODIS. *J. Geophys. Res.* **1998**, *103*, 32141–32157. [CrossRef]
35. Platnick, S.; Meyer, K.G.; King, M.D.; Wind, G.; Amarasinghe, N.; Marchant, B.; Arnold, G.T.; Zhang, Z.; Hubanks, P.A.; Holz, R.E.; et al. The MODIS cloud optical and microphysical products: Collection 6 updates and examples from Terra and Aqua. *IEEE Trans. Geosci. Remote Sens.* **2017**, *55*, 502–525. [CrossRef]
36. Frey, R.A.; Ackerman, S.A.; Liu, Y.; Strabala, K.I.; Zhang, H.; Key, J.R.; Wang, X. Cloud detection with MODIS. Part I: Improvements in the MODIS cloud mask for collection 5. *J. Atmos. Ocean. Technol.* **2008**, *25*, 1057–1072. [CrossRef]
37. Baum, B.A.; Menzel, W.P.; Frey, R.A.; Tobin, D.C.; Holz, R.E.; Ackerman, S.A.; Heidinger, A.K.; Yang, P. MODIS cloud-top property refinements for collection 6. *J. Appl. Meteorol. Climatol.* **2012**, *51*, 1145–1163. [CrossRef]

38. Ackerman, S.A.; Holz, R.E.; Frey, R.; Eloranta, E.W.; Maddux, B.C.; McGill, M. Cloud detection with MODIS. Part II: Validation. *J. Atmos. Ocean. Technol.* **2008**, *25*, 1073–1086. [CrossRef]
39. McGill, M.J.; Vaughan, M.A.; Trepte, C.R.; Hart, W.D.; Hlavka, D.L.; Winker, D.M.; Kuehn, R. Airborne validation of spatial properties measured by the CALIPSO lidar. *J. Geophys. Res.* **2007**, *112*, D20201. [CrossRef]
40. Weisz, E.; Li, J.; Menzel, W.P.; Heidinger, A.K.; Kahn, B.H.; Liu, C.-Y. Comparison of AIRS, MODIS, CloudSat and CALIPSO cloud top height retrievals. *Geophys. Res. Lett.* **2007**, *34*, L17811. [CrossRef]
41. Hagihara, Y.; Okamoto, H.; Luo, Z.J. Joint analysis of cloud top heights from CloudSat and CALIPSO: New insights into cloud top microphysics. *J. Geophys. Res. Atmos.* **2014**, *119*, 4087–4106. [CrossRef]
42. Haynes, J.M.; Stephens, G.L. Tropical oceanic cloudiness and the incidence of precipitation: Early results from CloudSat. *Geophys. Res. Lett.* **2007**, *34*, L09811. [CrossRef]
43. Kim, S.-W.; Chung, E.-S.; Yoon, S.-C.; Sohn, B.-J.; Sugimoto, N. Intercomparisons of cloud-top and cloud-base heights from ground-based lidar, CloudSat and Calipso measurements. *Int. J. Remote Sens.* **2011**, *32*, 1179–1197. [CrossRef]
44. Zhang, C.; Wang, Y.; Lauer, A.; Hamilton, K.; Xie, F. Cloud base and top heights in the Hawaiian region determined with satellite and ground-based measurements. *Geophys. Res. Lett.* **2012**, *39*, L15706. [CrossRef]
45. Juvik, J.O.; Nullet, D. Comments on "a proposed standard fog collector for use in high-elevation regions". *J. Appl. Meteorol.* **1995**, *34*, 2108–2110. [CrossRef]
46. Baumgardner, D.; Kok, G.; Dawson, W.; O'Connor, D.; Newton, R. A new groundbased precipitation spectrometer: The meteorological particle sensor (MPS). In Proceedings of the 11th Conference on Cloud Physics, Ogden, UT, USA, 2–7 June 2002.
47. Knollenberg, R.G. The optical array: An alternative to scattering or extinction for airborne particle size determination. *J.Appl. Meteorol.* **1970**, *9*, 86–103. [CrossRef]
48. Sun, B.; Karl, T.R.; Seidel, D.J. Changes in cloud-ceiling heights and frequencies over the United States since the early 1950s. *J. Clim.* **2007**, *20*, 3956–3970. [CrossRef]
49. ASOS Program Office Staff. *Automated Surface Observing System Users Guide*; ASOS Program Office, National Weather Service: Silver Spring, MD, USA, 1998.
50. Testik, F.Y.; Barros, A.P. Toward elucidating the microstructure of warm rainfall: A survey. *Rev. Geophys.* **2007**, *45*, RG2003. [CrossRef]
51. Barros, A.P.; Prat, O.P.; Shrestha, P.; Testik, F.Y.; Bliven, L.F. Revisiting low and list (1982): Evaluation of raindrop collision parameterizations using laboratory observations and modeling. *J. Atmos. Sci.* **2008**, *65*, 2983–2993. [CrossRef]
52. Testik, F.Y.; Barros, A.P.; Bliven, L.F. Toward a physical characterization of raindrop collision outcome regimes. *J. Atmos. Sci.* **2011**, *68*, 1097–1113. [CrossRef]
53. Barros, A.P.; Joshi, M.; Putkonen, J.; Burbank, D.W. A study of the 1999 monsoon rainfall in a mountainous region in central Nepal using TRMM products and rain gauge observations. *Geophys. Res. Lett.* **2000**, *27*, 3683–3686. [CrossRef]
54. Wilson, A.M.; Barros, A.P. Orographic land-atmosphere interactions and the diurnal cycle of low level clouds and fog. *J. Hydrometeorol.* **2017**, *18*, 1513–1533. [CrossRef]
55. Prat, O.P.; Barros, A.P.; Williams, C.R. An intercomparison of model simulations and VPR estimates of the vertical structure of warm stratiform rainfall during TWP-ICE. *J. Appl. Meteorol. Climatol.* **2008**, *47*, 2797–2815. [CrossRef]
56. Pinsky, M.; Khain, A.; Shapiro, M. Stochastic effects of cloud droplet hydrodynamic interaction in a turbulent flow. *Atmos. Res.* **2000**, *53*, 131–169. [CrossRef]
57. Pinsky, M.; Khain, A.; Krugliak, H. Collisions of cloud droplets in a turbulent flow. Part V: Application of detailed tables of turbulent collision rate enhancement to simulation of droplet spectra evolution. *J. Atmos. Sci.* **2008**, *65*, 357–374. [CrossRef]
58. Angulo-Martínez, M.; Barros, A.P. Measurement uncertainty in rainfall kinetic energy and intensity relationships for soil erosion studies: An evaluation using parsivel disdrometers in the southern Appalachian mountains. *Geomorphology* **2015**, *228*, 28–40. [CrossRef]
59. Del Genio, A.D.; Wolf, A.B. The temperature dependence of the liquid water path of low clouds in the southern great plains. *J. Clim.* **2000**, *13*, 3465–3486. [CrossRef]
60. Doran, J.C.; Zhong, S. Variations in mixed-layer depths arising from inhomogeneous surface conditions. *J. Clim.* **1995**, *8*, 1965–1973. [CrossRef]

61. Holz, R.E.; Ackerman, S.A.; Nagle, F.W.; Frey, R.; Dutcher, S.; Kuehn, R.E.; Vaughan, M.A.; Baum, B. Global moderate resolution imaging spectroradiometer (MODIS) cloud detection and height evaluation using CALIOP. *J. Geophys. Res.* **2008**, *113*, D00A19. [CrossRef]
62. Barros, A.P.; Lettenmaier, D.P. Incorporation of an evaporative cooling scheme into a dynamic model of orographic precipitation. *Mon. Weather Rev.* **1994**, *122*, 2777–2783. [CrossRef]
63. Barros, A.P.; Kuligowski, R.J. Orographic effects during a severe wintertime rainstorm in the appalachian mountains. *Mon. Weather Rev.* **1998**, *126*, 2648–2672. [CrossRef]
64. Maddux, B.C.; Ackerman, S.A.; Platnick, S. Viewing geometry dependencies in MODIS cloud products. *J. Atmos. Ocean. Technol.* **2010**, *27*, 1519–1528. [CrossRef]
65. Testik, F.Y. Outcome regimes of binary raindrop collisions. *Atmos. Res.* **2009**, *94*, 389–399. [CrossRef]